PAPER

Check for updates

Laser writing of metal-oxide doped graphene films for tunable sensor applications†

Shasvat Rathod, [ID] Monika Snowdon, [ID] Matthew Peres Tino [ID] and Peng Peng*

Flexible and wearable devices play a pivotal role in the realm of smart portable electronics due to their diverse applications in healthcare monitoring, soft robotics, human–machine interfaces, and artificial intelligence. Nonetheless, the extensive integration of intelligent wearable sensors into mass production faces challenges within a resource-limited environment, necessitating low-cost manufacturing, high reliability, stability, and multi-functionality. In this study, a cost-effective fiber laser direct writing method (fLDW) was illustrated to create highly responsive and robust flexible sensors. These sensors integrate laser-induced graphene (LiG) with mixed metal oxides on a flexible polyimide film. fLDW simplifies the synthesis of graphene, functionalization of carbon structures into graphene oxides and reduced graphene oxides, and deposition of metal-oxide nanoparticles within a single experimental laser writing setup. The preparation and surface modification of dense oxygenated graphene networks and semiconducting metal oxide nanoparticles (CuO_x, ZnO_x, FeO_x) enables rapid fabrication of LiG/MO_x composite sensors with the ability to detect and differentiate various stimuli, including visible light, UV light, temperature, humidity, and magnetic fluxes. Further, this *in situ* customizability of fLDW-produced sensors allows for tunable sensitivity, response time, recovery time, and selectivity. The normalized current gain of resistive LiG/MO_x sensors can be controlled between −2.7 to 3.5, with response times ranging from 0.02 to 15 s, and recovery times from 0.04 to 6 s. Furthermore, the programmable properties showed great endurance after 200 days in air and extended bend cycles. Collectively, these LiG/MO_x sensors stand as a testament to the effectiveness of fLDW in economically mass-producing flexible and wearable electronic devices to meet the explicit demands of the Internet of Things.

1 Introduction

Wearable electronics play a pivotal role in seamlessly integrating us and our environment through flexible sensor systems and wireless connectivity. Over the past decade, substantial efforts have been dedicated to creating versatile human-interactive devices that mimic skin-like functions, such as sensing touch, humidity, or temperature.[1–4] While traditional planar integrated-circuit devices are sophisticated, their rigidity and fragility render them unsuitable for the soft and curvilinear forms of the human body. In contrast, flexible wearable electronics, which are bendable and adapt to the body without causing discomfort, enable a broad spectrum of sensing functionalities.[1,5,6] In recent years, nanostructures composed of metal oxides (MO), including Co_3O_4, Cu_2O, Fe_2O_3, In_2O_4, TiO_2,

Centre for Advanced Materials Joining, Department of Mechanical and Mechatronics Engineering, University of Waterloo, 200 University Avenue West, Waterloo, Ontario, N2L 3G1, Canada. E-mail: peng.peng@uwaterloo.ca

† Electronic supplementary information (ESI) available: fLDW technical process; electron transport mechanism on rGO sheets; crumpling in rGO sheets; shapelets code mathematical computation and python GitHub (Fig. S1 and S2); resistive sensing mechanism in MO_x. See DOI: https://doi.org/10.1039/d4na00463a

SnO_2, WO_3, and ZnO, have gained widespread attention in sensing due to their exceptional chemical stability, mechanical flexibility, and substantial specific surface area.[7–10] These metal oxide nanoparticles are particularly favored for applications in light sensing and gas sensing because they are biosafe, biodegradable, and biocompatible.[4,8,9] Furthermore, high-performance room temperature sensors are also possible by hybridizing metal oxides with graphene to enhance charge transport.[11]

Likewise, graphene oxide (GO), stands out for its rich content of oxygen functionalities, rendering it electronegative and facilitating the fixation of metal cations on its surface through electrostatic interaction or chemical bonding.[7,12] Additionally, the rigid surface of GO serves as an ideal substrate for nucleation, crystal growth, and the formation of ultrafine nanostructures with homogeneous dispersion and controlled morphologies.[12–14] The presence of oxygen functional groups on the material surface enhances the electron and charge transfer rate, rendering GO water-soluble and biocompatible.[15] Upon reduction, GO transforms into reduced graphene oxide (rGO), retaining some residual oxygen and structural defects. rGO exhibits remarkable thermal conductivity comparable to doped conductive polymers,[16] approximately 36 times higher than Si and roughly 100

times higher than GaAs.[17] Furthermore, rGO provides tunable electrical properties for specific applications through the functionalization of oxygen groups. Consequently, rGO holds tremendous potential as a cost-effective alternative to Si and metal-based sensors.[18] However, despite its promising attributes, the practical application of rGO sensors is currently confined to research laboratories and has not yet transitioned to the market.[15,19,20] One of the challenges dragging this transition is the rapid, cost-effective, and large-scale industrial production of these sensors.[21] Currently, the conventional methods for producing rGO provide limited yield of graphene oxide. Many sensors incorporating rGO composites predominantly rely on electrochemical methods, which, though effective, present challenges in terms of cost and environmental longevity.[8,9] A seamless process to combine rapid GO/rGO film fabrication with metal oxide nanoparticle deposition on flexible substrates can revolutionize the mass production of wearable flexible sensors.

In this investigation, a simple fiber laser direct writing (fLDW) process is employed to produce flexible graphene sensors with MO nanoparticles. fLDW is a one-step consolidation of multiple printing processes.[9] This singular process can effectively (i) synthesize graphene, (ii) optimize the performance of carbon structures through functionalization, (iii) perform p– or n–doping and hybridization, and (iv) deposit metal-oxide nanoparticles. The variation of laser writing parameters allows for the modification of the LiG surface, its functional group concentrations, and MO nanoparticle concentrations, thereby elevating, or obstructing the electrical and optoelectronic properties of the LiG/MO_x sensors. Consequently, the fabricated LiG/MO_x sensors offer exceptional controllability in selectivity, response time, recovery time, reproducibility, and stability. The formation of LiG/MO_x sensors and their performance will also be evaluated by in-depth characterizations. As a proof of concept, flexible sensor responses to various elemental stimuli, such as temperature gradients, visible light, UV light, magnetic fluxes, and humidity will be demonstrated.

2 Materials and methods

Kapton® was purchased from McMaster-Carr. The polymer is produced through a polycondensation reaction between pyromellitic dianhydride (PMDA) and 4,4′-diaminodiphenyl ether (ODA). The resulting imide groups (–CO–N–CO–) in the polymer structure enable laser irradiation to convert the polyimide into graphene and graphene oxide compounds.

The precursor ink was prepared following the procedure by Rathod *et al.*[22,23] This process involved dissolving 2 M polyethylene glycol (PEG, Sigma Aldrich, 8000 mol. wt., 99% purity), 2 M polyvinylpyrrolidone (PVP, Sigma Aldrich, ~110 μm particle size, mol. wt. 120, 99% purity), and 2 M copper nitrate (Sigma Aldrich, trihydrate, mol. wt. 241, 99% purity) or 2 M zinc nitrate hexahydrate (Sigma Aldrich, mol. wt. 297.49, 99% purity) or 2 M iron nitrate (Sigma Aldrich, nonahydrate, mol. wt. 404, 99% purity) in deionized (DI) water. The MO_x solutions are made in volumetric ratios of 5 : 1 : 1 : 3 with deionized water, polyethylene glycol 0.2 g mL^{-1}, polyvinyl pyrrolidone 0.1 g mL^{-1}, and respective metal nitrates (copper nitrate, zinc nitrate, and

iron nitrate). The solution was sonicated for 15 minutes until homogeneity. Deposition of the MO_x nanoparticle solution, onto the PI substrate, was achieved through a spray pump bottle. The DynalonTM Quick MistTM HDPE Sprayer bottles provide a fine mist of roughly 1/22 mL, sprayed from a distance of 15 cm from the PI substrate.

fLDW was performed using a YLR-30-MM-AC IPG continuous wavelength fiber laser within a MIYACHI MX2000 Glovebox. The laser, operating at 1070 nm, has a maximum output power of 30 W and a spot diameter of 500 μm.

The fabricated materials underwent comprehensive electrical and optoelectronic characterization using a Keithley 4200A semiconductor parameter analyzer (Tektronik, Beaverton, OR USA). The morphologies and compositions of the induced patterns were assessed through scanning electron microscopy (SEM, Zeiss FESEM 1530, Carl Zeiss, Munich, Germany) equipped with energy dispersive spectroscopy (EDS, VGS ESCALab, ThermoFischer Scientific). For sensor response tests under light and UV light conditions, a Dicuno© 5 mm light-emitting diode, "warm blue", emitting at a wavelength of 625 nm, with electrical properties of 20 mA, 3–3.2 V, and 12 000–32 000 mcd was utilized. Additionally, a red LED emitting at a wavelength of 700 nm, with electrical properties of 20 mA, 2–2.2 V, and 2000–3000 mcd, and a UV LED at a wavelength of 395 nm, with electrical properties of 20 mA, 3–3.2 V, and 600–800 mcd were employed for the tests. For sensor response tests related to magnetic field fluxes, two standard ring magnets with a radius (r) of 0.05 m, width (w) of 0.03 m, remanence (Br) of 1.06 T, and a calculated magnetic flux density of 10^{-4} T at a distance of 5 cm from the sensor were used. Humidity tests were conducted in a humidity chamber set at 95% humidity. Bend tests were performed with a NEMA 12-step motor and a 3D printed holder with a bend radius of 4.02 mm and strain of 0.7% for the monolayer model. X-ray photoelectron spectroscopy (XPS, VGS ESCALab 250 Imaging ESCA, Thermo Fischer Scientific, Waltham, MA USA) was performed, and data were analyzed using CASAXPS. X-ray diffraction (XRD, PANalytical X'pert Pro MRD HR-XRD, Malvern Panalytical, Malvern UK) was conducted and analyzed using Match! Software (Crystal Impact, Bonn, Germany) using a standard 2Theta-omega scan from 10–90°.

3 Results and discussion

3.1 Composition of LiG/MO_x films

Fig. 1a illustrates the fabrication procedure employed for the production of flexible LiG/MO_x nanoparticle sensors on polyimide (PI) substrates, adapted from Rathod *et al.*[22,23] First, the PI film undergoes irradiation/ablation using a fiber laser to generate porous LiG films – the application of high laser energy density during laser ablation results in the cleavage of C–O, C=O, and C–N bonds.[15] Subsequently, the newly discharged carbon atoms rearrange to form a graphene structure or gases. Furthermore, fLDW under ambient atmospheres can introduce oxygen functional groups on the induced graphene structures.[22] As a result, the porosity, density, and conductivity nature of LiG are adjustable by varying the laser parameters. Second, the precursor ink is sprayed onto the newly formed LiG films,
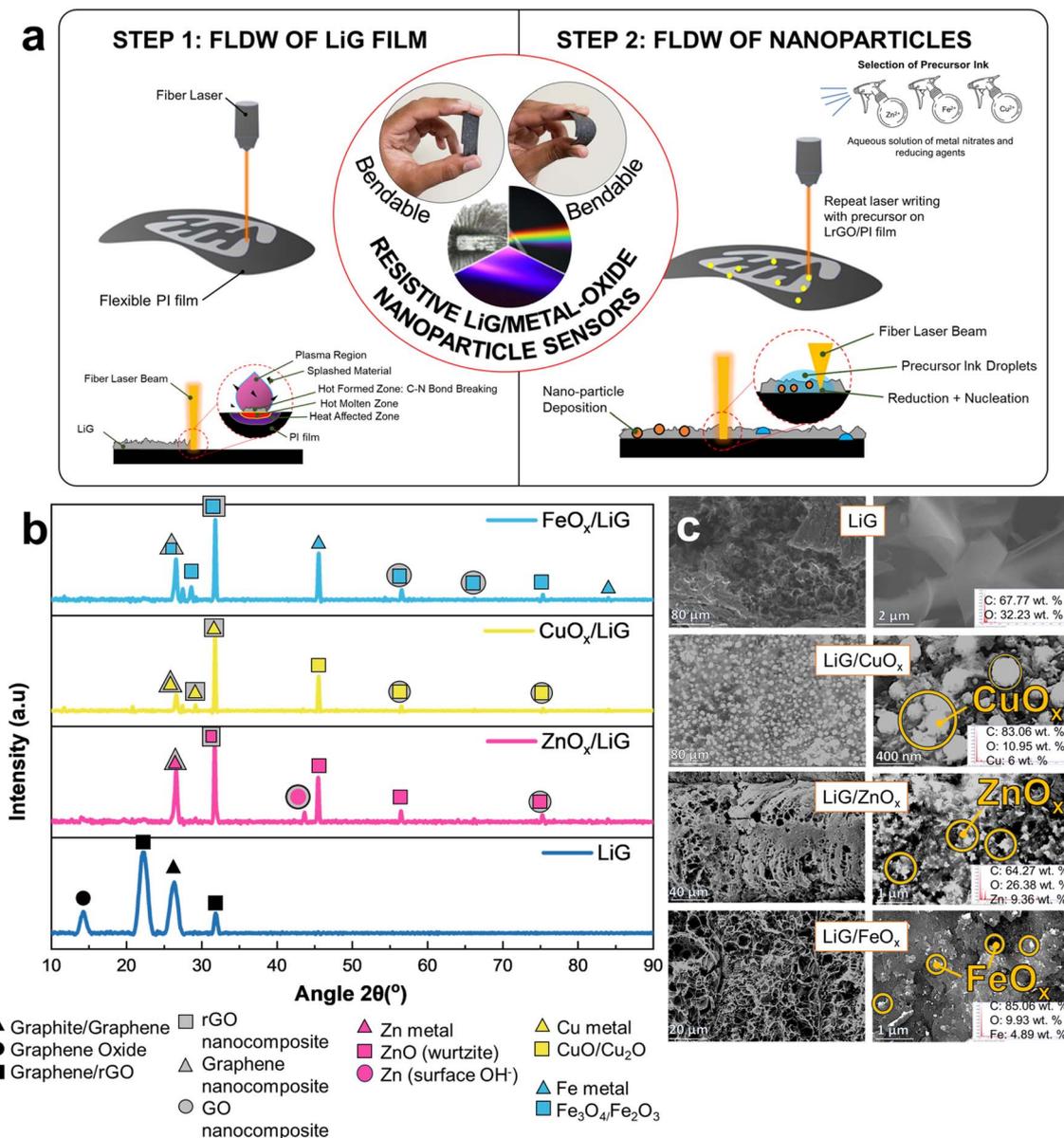
Fig. 1 (a) Fabrication mechanism and schematic of LiG/MO$_x$ sensor with fLDW. (b) XRD spectra analysis and (c) SEM images with EDS results of LiG/MO$_x$ films.

followed by another round of laser scanning. Cu(NO$_3$)$_2$, Fe(NO$_3$)$_2$, and Zn(NO$_3$)$_2$ are used in the precursor ink interchangeably to deposit CuO$_x$, FeO$_x$, and ZnO$_x$ nanoparticles, respectively. Similar to the LiG film, and well-documented, the composition of the metal/metal oxide deposits can be modified by varying laser processing parameters.[10,15,24–26]

XRD analyses presented in Fig. 1b show the structural characteristics of LiG films, revealing their amorphous nature with discernible phases of small graphite, graphene oxide, and reduced graphene oxide. Specifically, a prominent peak at $2\theta = 26.62°$ along the (002) plane is observed for graphite.[27] The peak at $2\theta = 14.5°$ indicates partial oxidation of graphite phases to GO.[27–29] Additionally, broader peaks at $2\theta = 24.10°$ signify the presence of rGO.[19,30] Furthermore, a diffraction peak is observed

at $2\theta = 32°$, which is caused by the reduction of graphene oxides.[31] On the other hand, in the XRD spectra for LiG/MO$_x$ films, the characteristic peak of graphene oxide at $2\theta = 14°$ is notably absent, replaced by sharper graphite and rGO oxide peaks, particularly a sharper peak corresponding to graphite/rGO at $2\theta = 32°$. Generally, a greater intensity of the 32° peak indicates a fully graphitic system.[32] This observation suggests that during the initial laser pass, fLDW predominantly deposits GO, which undergoes treatment to form rGO/Gr after secondary passes[31,33] due to a precipitation reaction with metal ions from the precursor ink.[33] Thus, fLDW can deposit multiple forms of graphite, graphene, graphite oxides and graphene oxides.

In the case of LiG/ZnO$_x$ films, a characteristic rGO/ZnO nanocomposite peak at $2\theta = 32°$ is observed, alongside a Gr/

Zn phase peak at $2\theta = 26°$.[34] Furthermore, three distinct diffraction peaks are present, separate from LiG peaks, at 43.5°, 45.5°, and ~56°. First, an additional non-characteristic peak at ~44° could be a product of GO/Zn-metal composites or symptomatic of the presence of surface hydroxyls in ZnO; a byproduct of fLDW in ambient air conditions.[35] Second, peaks at $2\theta = 45.5°$ and $2\theta = 56.5°$ are characteristic of a hexagonal wurtzite structure of ZnO at planes (102) and (110), respectively. A minor peak is present highlighting the presence of GO/ZnO nanocomposites at $2\theta = 75.5°$. The calculated composition breakdown through Rietveld refinement is 93 at. % ZnO and 7 at. % metallic Zn (JCPDS: 36-1451).[36,37]

Similarly, CuO_x nanoparticle deposition on LiG showed mixed Gr/CuO/Cu_2O phases at $2\theta = (26°, 27°, 29°, 32°, 44°,$ and 56°). The peaks at $2\theta = 26°$ and $2\theta = 27°$ correspond to the presence of carbon/copper-oxide composites with graphene and rGO phases, respectively.[38,39] Notably, the graphene peak at $2\theta = 26°$ is significantly less defined for CuO_x than ZnO_x depositions, suggesting a lower weight ratio of graphene to copper than graphene to zinc.[34] This discrepancy may arise from the fLDW process, wherein the metal and metal-oxide nanoparticles are induced by reducing ions present in the precursor solution. Because copper has a higher reduction potential compared to zinc, it tends to be induced more readily. Consequently, this leads to a lower ratio of graphene to copper in the resulting composite material. Peak $2\theta = 32°$, as aforementioned, is indicative of rGO/metal–Cu phases in the LiG/CuO_x film.[40] All discernible peaks associated with copper indicate the polycrystalline nature of the resulting product.[41] Specifically, the distinct cuprous oxide peak at $2\theta = 29°$ and the metallic fcc-Cu peak at $2\theta = 44°$ align with the (110) and (111) phases, respectively.[42,43] Furthermore, minor but discernible peaks at $2\theta = 56.5°$ and $2\theta = 74.5°$ are observed in GO/CuO nanocomposite structures.[44] Rietveld refinement through Match! Calculates a composition of 53.8 at. % CuO, 24 at. % Cu_2O, and 22.2 at. % Cu (JCPDS 04-0836).[45,46]

Likewise, LiG/FeO_x XRD analysis indicates the presence of mixed graphene and Fe metal, Fe_3O_4, Fe_2O_3/FeO peaks at $2\theta = (26°, 27°, 29°, 32°, 46°, 56°,$ and 75°). In the case of nanoparticles, it is difficult to distinguish between magnetite Fe_3O_4 and maghemite γ-Fe_2O_3 phases, solely from XRD. Peaks corresponding to Gr/FeO_x and rGO/Fe_3O_4 nanocomposites are evident at $2\theta = 26°$ and $2\theta = 32°$, respectively.[47–50] At $2\theta = \sim27–29°$, a characteristic rhombohedral hematite α-Fe_2O_3 phase was observed, previously found to appear in GO/FeO_x nanocomposites annealed at extremely high temperatures.[49] A characteristic iron peak at $2\theta = 46°$ is clearly present.[51] Whereas weaker peaks are observed at 56°, 66°, 74°, and 84°; denoting GO/FeO_x nanocomposite, GO/Fe_3O_4 nanocomposite, magnetite Fe_3O_4, and Fe phases, respectively.[34,48–52] The smaller Fe_2O_3 peaks imply fLDW deposition through the reduction of Fe ions to Fe_2O_3 magnetic nanoparticles (MNPs) to further reductions into Fe_3O_4.[53] Rietveld refinement confirms nanoparticle composition of 91.5 at. % Fe_3O_4 and 8 at. % Fe (JCPDS No. 75-0033, 39-1346, 90-2377).[54]

Overall, the XRD analysis provides compelling evidence of graphene and nanoparticle deposition and graphene-metal/MO bonding. However, the presence of multiple phases of graphene and various phases of selected nanoparticles complicates the precise determination of their exact states. SEM and EDS results summarized in Fig. 1c highlight the presence of metal and metal oxide nanoparticle depositions after step two of fLDW ranging in size and localized concentrations. Visually, there is a pronounced affinity of metal nucleation at defect sites.[55–57] At low magnifications, concentrated NP deposits are observed at the porous edges of the LiG film.

3.2 Effects of p-type and n-type LiG films

The fLDW process allows for the production of sensors with tailored responses to external stimuli, by guiding electron movement on rGO sheets, as shown in Fig. 2a. A breakdown of the mechanisms involved is briefly discussed in ESI Section 1.† Fig. 2b highlights the sensing mechanism for n-type and p-type metal-oxide sensors (MOSs). In LiG/MO_x sensors, the response is governed by the conductive properties of the LiG film, thereby influencing the overall sensing behavior.

XRD spectra reveal that increased laser energy results in decreased crystallinity of the LiG film. In Fig. 2c, the LiG film displays prominent peaks characteristic of graphene oxide at approximately 14° and 22° ($d = 0.822$ and 0.432 nm) at low energy. Conversely, with the high laser energy density of fabrication, these GO peaks become broader. Both films exhibit a graphite peak at 26.6° ($d = 0.335$ nm), albeit less noticeable at higher laser energy. The broader and smoother peaks suggest a greater presence of amorphous structures. Initially exhibiting n-type conductivity, GO transforms p-type rGO through the reduction of oxygen-donating groups, thereby inducing p-type conductivity.[22]

To evaluate the efficacy of fLDW in printing n-type and p-type LiG films, a hot probe test[58] was conducted on samples produced at varying laser energy densities. Below 2 J mm^{-3}, the process primarily deposits an n-type film; while between 2 and 2.5 J mm^{-3}, the LiG exhibits p-type characteristics. The conductivity nature can be controlled by modifying laser energy density as presented in Fig. 2d. This conductivity switch aligns with the surface functional groups on the LiG surface identified through XPS C 1s scans in Fig. 2e. At lower laser energy densities, the sample shows a higher ratio of electron-donating groups, marked by a higher ratio of C=O groups with a greater likelihood of lone pairs to donate.[59] A noticeable transition occurs at around 2 J mm^{-3}, where the ratio of C–N groups increases, exerting electron-withdrawing effects because the nitro groups, known for stable π bonds with electronegative atoms, contribute to this transition.[22,57,60–62] XPS spectra analysis concludes that fLDW effectively controls LiG film conductivity through surface modification of functional carbonyl and oxygen groups.[63]

A LiG/ZnO_x sensor was fabricated, and its response to UVA (1.085 W m^{-2}) under 1 V bias is shown in Fig. 2f. Upon activating the UV source at 2 seconds, the n-type LiG/ZnO_x sensor's normalized current gain increases by a factor of 1.7, while the p-type sensor's normalized current gain decreases by an equivalent factor. Thus, the response fLDW sensors can be effectively tuned positively or negatively by controlling the conductivity nature of the LiG films.
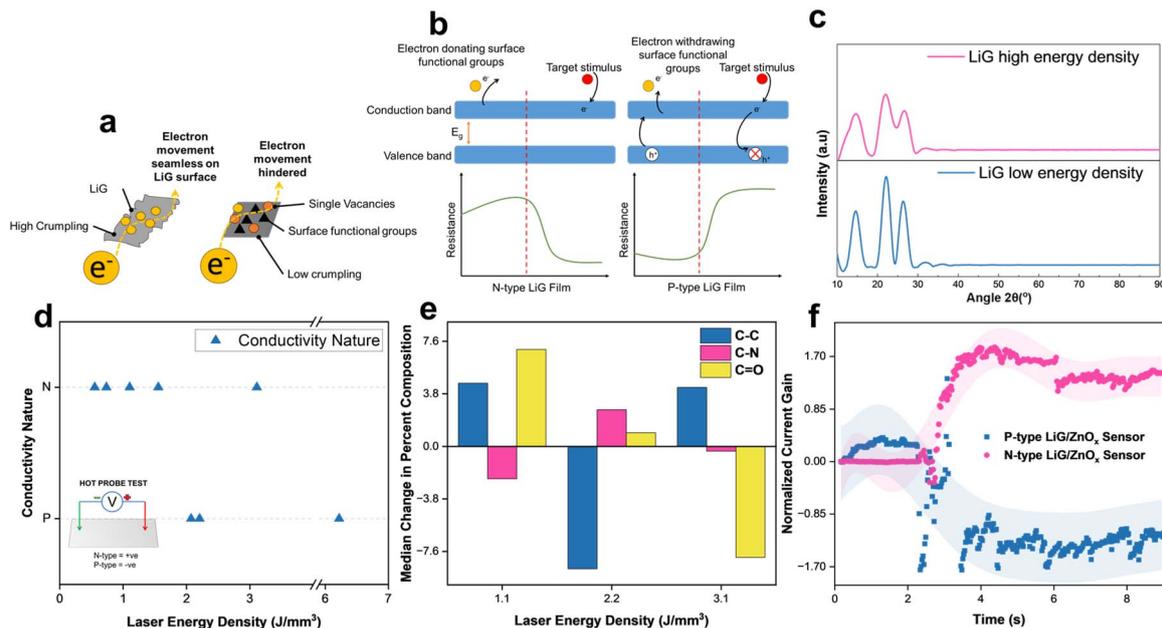
Fig. 2 (a) Schematic of electron transport modification on LiG film. (b) Resistive metal-oxide sensing mechanism for p-type and n-type LiG. (c) XRD spectra of GO and rGO films produced through fLDW (d) Laser energy density *vs.* Conductivity nature of induced LiG films. (e) Laser energy density *vs.* change in functional groups, data educed from XPS C 1s scans. (f) Time *vs.* normalized current gain of P-type and N-type LiG/ZnO$_x$ samples under 1 V bias and UV stimulus.

3.3 Effects of sp^2 carbon hybridization in LiG films

In addition to controlling conductivity nature, fLDW has the capability to modify the morphology of disordered regions in the LiG film, thereby influencing the mobility of charge carriers, as illustrated in Fig. 3. ESI Section 2† details electron transport mechanisms on rGO films. Fig. 3a and b demonstrates that laser energy density regulates sp^2 carbon formations on LiG, which directly influences electron hopping.
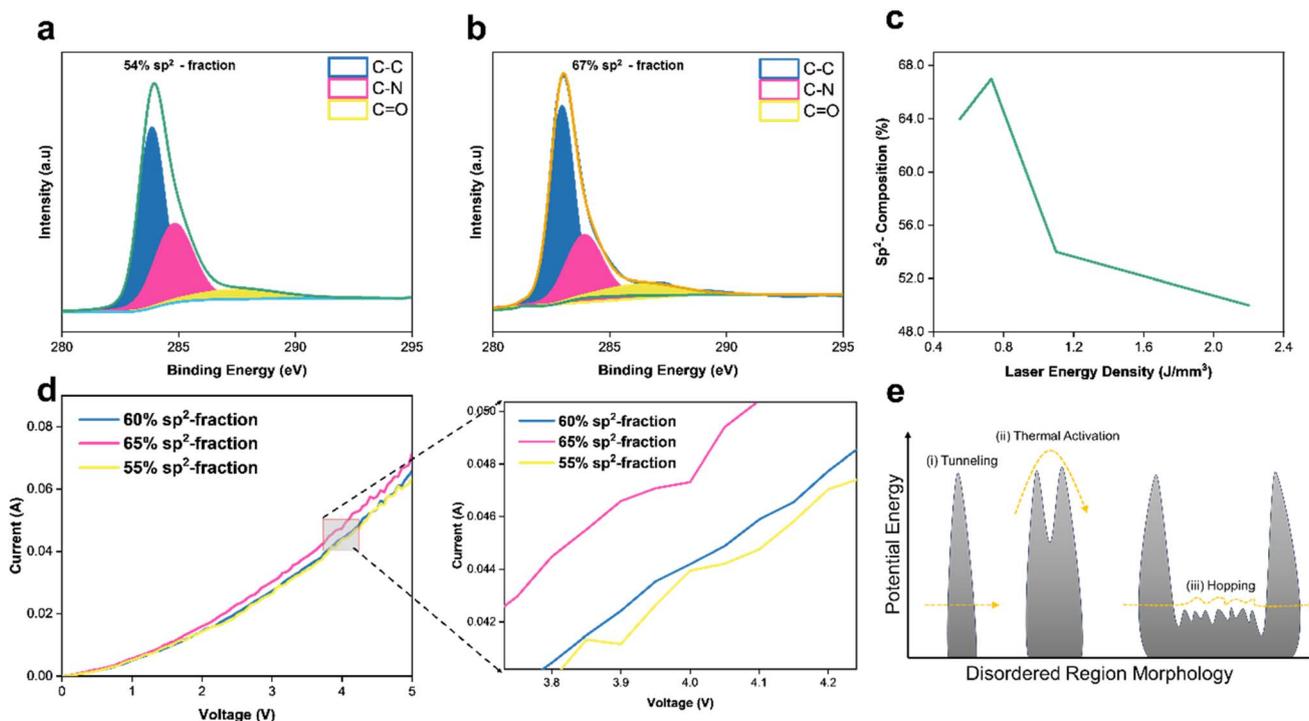

Fig. 3 (a) XPS C 1s scan of a high energy density 1.2 (J mm^{-3}) LiG film. (b) XPS C 1s scan of low energy density 0.8 (J mm^{-3}) LiG film. (c) Laser energy density of fLDW process *vs.* sp^2 fraction. (d) *I–V* curve of LiG films with increasing sp^2 C−C fraction. (e) Electron hopping mechanism on GO surface morphology.
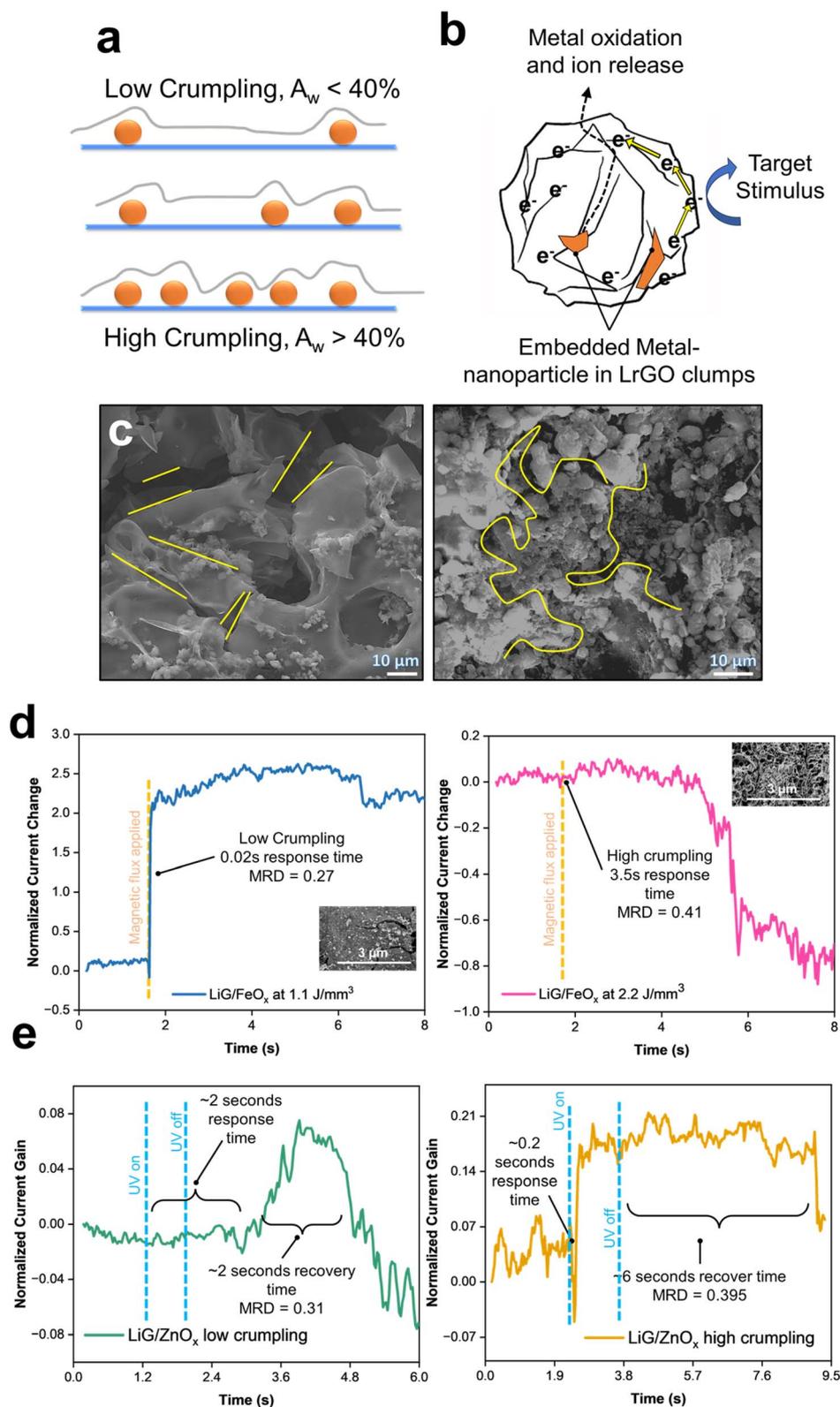
Fig. 4 (a) Nano-particle induced crumpling of rGO mechanism in LiG/MO$_x$ films. (b) Sensing mechanism in crumpled rGO sheets with MO nanoparticles. (c) SEM image of LiG crumpling after nanoparticle deposition, low laser energy density (left), and high laser energy density (right). Time *vs.* change in current output of (d) LiG/FeO$_x$ and (e) LiG/ZnO$_x$ with different rGO crumpling.

Three discernible peaks are highlighted: sp^2-carbon (peak C–C), defect/sp^3-carbon (C–N), and bonds of carbonyls (C=O). The sp^2-carbon fraction, indicative of higher Hall mobility, is determined by multiplying the percentage of total carbon from C 1s bond values identified by XPS spectra. fLDW conducted at lower energy densities result in a higher fraction of sp^2 carbons as evidenced by XPS C 1s spectra of LiG films induced at 1.2 J mm^{-3} and 0.8 J mm^{-3} respectively (and compiled on the I–V curve in Fig. 3c). Fig. 3d confirms a higher fraction of sp^2 carbon corresponds to lower resistance due to a greater electron movement facilitated by an increase in the hopping Hall mobility of charge carriers.[64] At a 4 V bias, the LiG film with a 60% sp^2 fraction exhibits a 4.9% higher current output than the 55% sp^2 fraction film. Thus, fLDW holds promise for tuning electrical properties in LiG/MO_x sensors by controlling the fraction of sp^2 carbon. Usually, the reduction of rGO increases the sp^2 carbon fraction, reducing resistivity and enhancing charge carrier mobility[61,65] due to range hopping, as shown in Fig. 3e. The low potential barriers between crystalline sp^2 domains and disordered regions offer lower resistance and greater electron mobility.[66]

3.4 Effects of LiG film crumpling

During step two of laser scanning (Fig. 1a), the initial LiG layer could undergo variable deforming forces caused by the plasma plume as it travels across the LiG surface inducing localized strains[67,68] leading to crumpling of LiG films. Detailed mechanisms are outlined in ESI Section 3.† This crumpling process can influence the electronic properties of tunable LiG/MO_x sensors by inducing magnetic fields, altering local potentials, and impacting electron mobility across the 3D graphene matrix.[19,69] As illustrated in Fig. 4a, the concentration and localization of nanoparticles can influence the crumpling affinity of LiG sheets. The presence of defects and electronegative nanoparticles leads to stronger folding due to the smaller distance between graphene and adhesion sites facilitated by van der Waals forces.[69–71] The crumpling in the porous LiG film could affect the metal-oxide nanoparticle sensing process, as shown in Fig. 4b. When metal oxides transfer electrons to graphene, equalizing Fermi levels and facilitating their transfer to internal carbon structures, it will enhance the oxygen reduction on the outer surface. This reaction would be accelerated if the transport through metal oxides is inherently slow.[72,73] Conversely, folded porous LiG sheets with high crumpling encase metal-oxide nanoparticles physically to separate oxide species from the metal-oxide cation release location, leading to a decelerated electron transport.[69,72,73] Thus, the overall effect of crumpling is determined by metal-oxide composition.

Fig. 4c illustrates the difference between a low-crumpled (left) and highly-crumpled (right) LiG film. On the left, the stacking of LiG sheets is evident with nanoparticles on the surface. However, as the laser energy is increased, the LiG sheets start coalescing to form distinct clumps. The bonds between MO_x and LiG bridge the electron transfer channels and tighten the connection between them, creating an affinity for metal agglomeration, increased structural stability, and defect zones which attract rGO sheets towards centralized locations.[74–76] Nonetheless, quantifying the extent of crumpling and correlating it to a specific laser energy density is somewhat difficult due to the complexities during fLDW deposition. To address the complexity, an image processing technique using shapelet functions called the response distance method[77] was modified to process SEM images of the LiG films to determine the mean response distance (MRD) which provides a linear correlation to crumpling. The shapelet-based code[78] and detailed explanation of crumpling mechanisms with XPS scan data correlations are provided in ESI Section 3.† Table S1† also summarizes the fractions of bonds between metal-oxide and LiG, and corresponding MRD (crumpling factors) for all the films at various laser energy densities.

Fig. 4d emphasizes the effect of crumpling on LiG/FeO_x sensors. Different LiG/FeO_x samples were fabricated at different laser energy densities, resulting in distinct levels of crumpling. The sample fabricated at 1.1 J mm^{-3} showed minimal crumpling (MRD = 0.27), in which an immediate response to the stimuli was achieved with a current gain factor of 2 under a magnetic flux of 10^{-4} T. On the other hand, the high porosity and crumpling sample (MRD = 0.41) at 2.2 J mm^{-3} exhibited
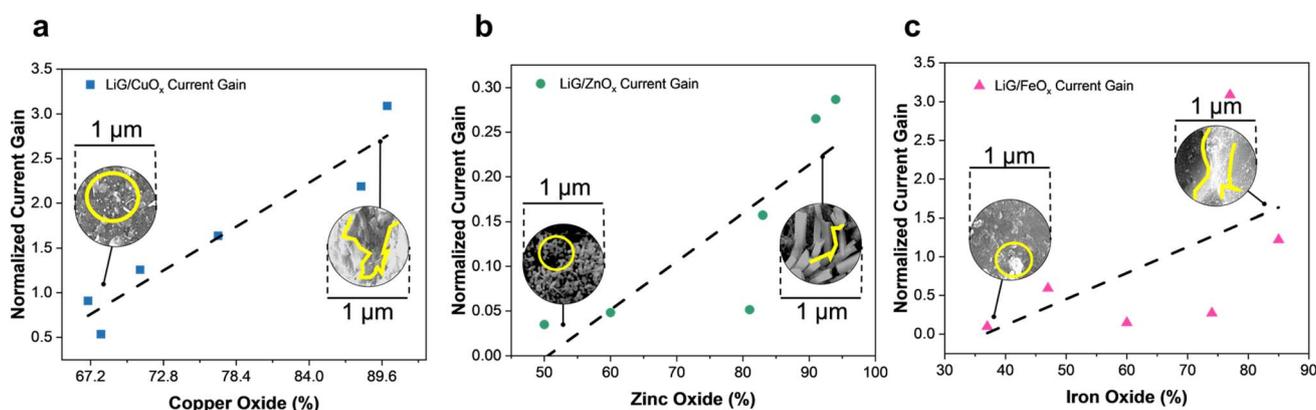

Fig. 5 Normalized current gain vs. metal oxide percentage extrapolated from XPS spectra of, (a) copper oxide film (b) zinc oxide and (c) iron oxide.

a significant increase in response time of 3.5 s from exposure to an equivalent magnetic field strength.

Furthermore, recovery time in LiG/ZnO$_x$ was observed under a short UV pulse of 1.085 W m^{-2} of 0.5 seconds, see Fig. 4e. The low crumpled LiG/ZnO$_x$ film (MRD = 0.31) took 2 seconds to respond to the UV pulse and displayed a 2 seconds recovery time after. In contrast, the highly-crumpled LiG/ZnO$_x$ film (MRD = 0.395) responded immediately within 0.2 seconds and required 6 seconds to recover. Interestingly, high crumpling has opposite effects on response time for FeO$_x$ and ZnO$_x$. Thus, the net effect of decelerating and accelerating nanoparticle oxidation, through rGO crumpling, is dependent on the metal-oxide species.[69,79]

3.5 Effects of metal oxide nanoparticles

The tunable band gap and the ability of 2D/3D graphene material to act as a molecular scaffold for metal/metal oxide
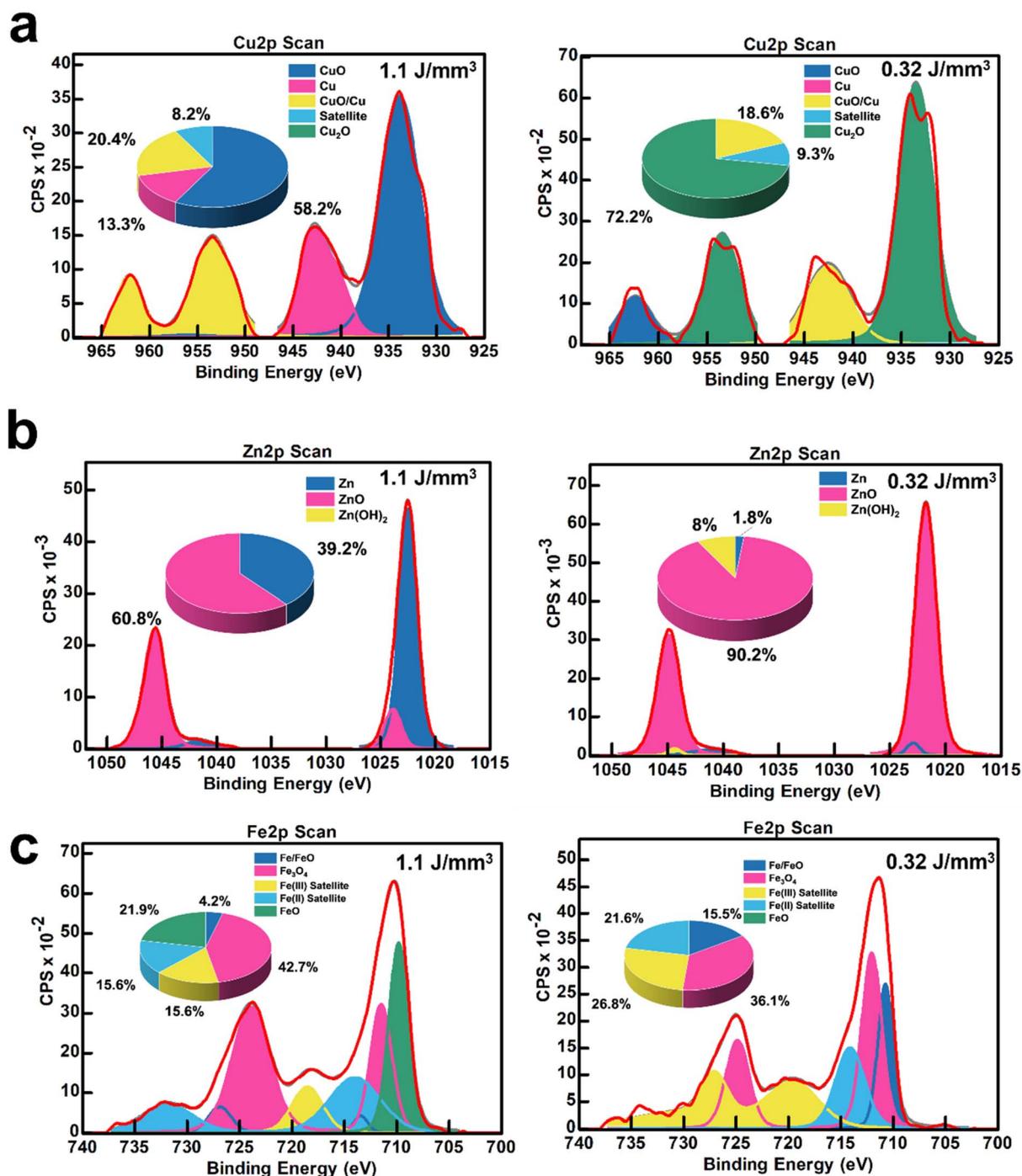

Fig. 6 (a) XPS Cu 2p scans of LiG/CuO$_x$ sensor films with high CuO and Cu$_2$O content; (b) XPS Zn 2p scans of LiG/ZnO$_x$ sensor films with different ZnO content; and (c) XPS Fe 2p scans of LiG/FeO$_x$ sensor films with different FeO$_x$ compositions.
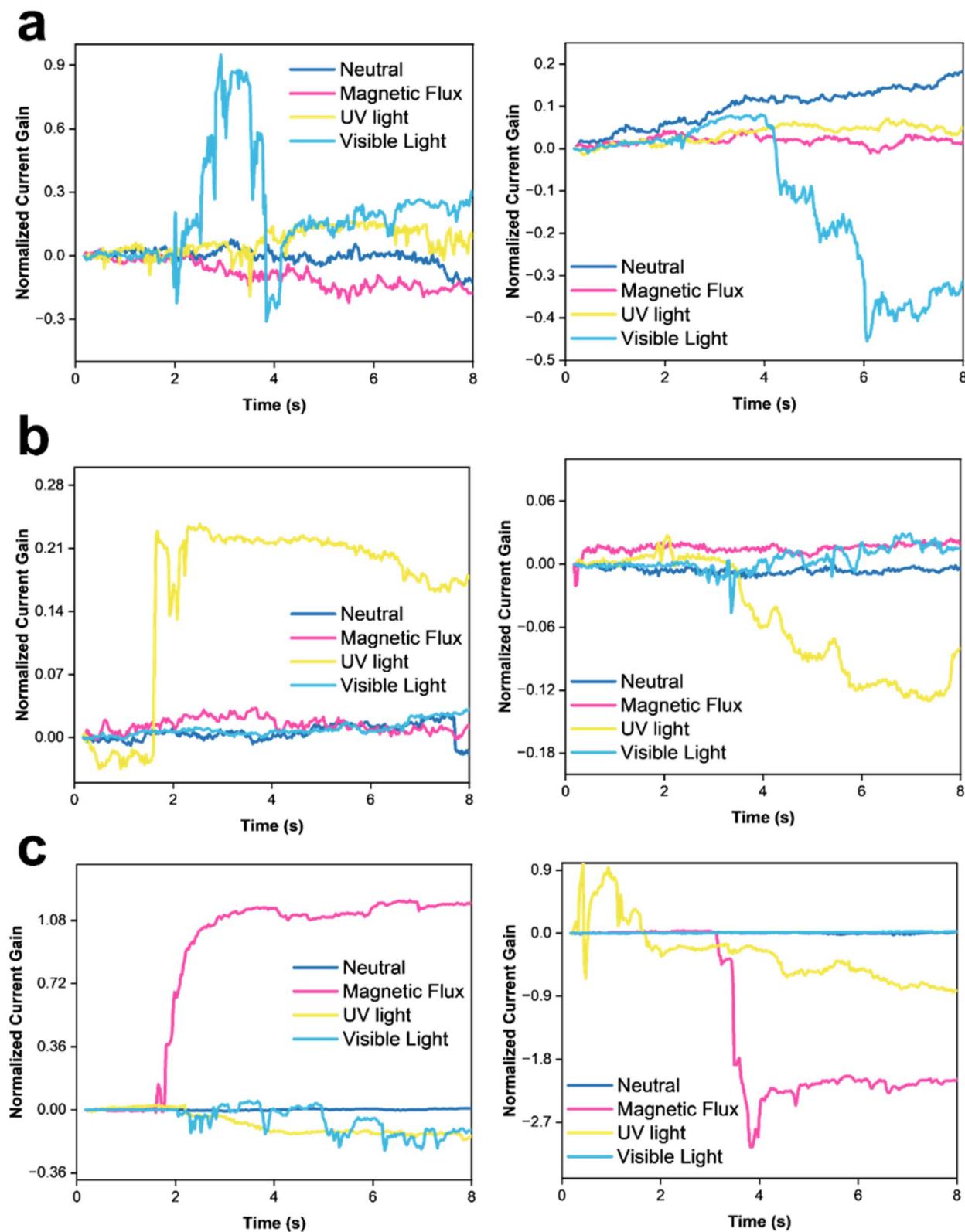
Fig. 7 $I-V$ curves of time *vs.* normalized change in current of (a) n-type LiG/CuO$_x$ sensor (left) and p-type LiG/CuO$_x$ (right), (b) n-type LiG/ZnO$_x$ sensor (left) and p-type LiG/FeO$_x$ sensor (right), and (c) n-type LiG/FeO$_x$ sensor (left) and p-type LiG/FeO$_x$ sensor (right).

nanoparticles can tune and enhance the electrical properties of resistive sensors.[7,55,57,72] ESI Section 4† details the resistive sensing mechanism of the oxides. Fig. 5 presents the tunable responsivity of different metal oxides laser-treated through fLDW. The oxide content was extrapolated from the XPS spectrum of metal in the films. In Fig. 5a, the current gain of LiG/CuO_x sensors is shown to increase with CuO_x content. The normalized current gain is defined as the change in sensor output of an n-type-LiG/CuO_x film under exposure to visible light of 1.5 W m^{-2} for 5 seconds. Furthermore, as highlighted in Fig. 5a, SEM images showed agglomerated CuO_x on the LiG surface. The flexibility of the fLDW process allows replacing CuO_x with ZnO_x by only changing the precursor contents during step two deposition. Similar to CuO_x a higher concentration of ZnO_x results in a greater normalized current gain when exposed to UV light of 1.085 W m^{-2} for 5 seconds as illustrated in Fig. 5b because ZnO_x relies on the photoelectric effect.[80] Lastly, the fLDW process was applied to deposit iron oxides on LiG as well. An n-type-LiG/FeO_x film under exposure to a magnetic flux of 10^{-4} T for 5 seconds exhibits greater response at higher FeO_x concentration due to particle agglomeration and greater contact points between graphene/metal-oxide composite, see Fig. 5c, similar to the other reported transition metal oxides.[81,82]

Fig. 6 highlights the ability to tune nanoparticle composition (metal and metal oxide atomic percentages) by adjusting the laser energy density (0.32 and 1.1 J mm^{-3}). XPS Cu 2p scans in Fig. 6a establish that fLDW can deposit a CuO-concentrated nanoparticle blend of 58.2 at% CuO, 20.4 at% CuO/Cu, and 13.3 at% Cu at high laser energy, which can be tuned to deposit a more Cu_2O concentrated (72.2 at%) composition at low energy. The level of reduction of the Cu ions in the precursor solution to Cu^{2+} and Cu^{+} can be effectively controlled by varying the laser energy density.[25] fLDW successfully deposited ZnO_x nanoparticles composed of 60.8 at% ZnO and 39.2 at% Zn metal at high laser energy density which could be changed to a composition of 90.2 at% ZnO and 8 at% Zn metal at low laser energy density, as shown in Fig. 6b. Therefore, the normalized current gain of a UV LiG/ZnO_x sensor can be effectively optimized by changing the surface concentration of ZnO in the LiG-

ZnO_x matrix. LiG/FeO_x sensors, as presented in Fig. 6c, show low energy density fabrication has a film composition breakdown of 15.5 at% Fe/FeO and 36 at% Fe_3O_4, whereas, the nanoparticles have a greater Fe_3O_4 composition of 42.7 at% and FeO/Fe metal of 4.2 at% at high energy density.

To identify the selectivity of the metal oxide nanoparticles in LiG/MO_x sensors, different stimuli were used, including a magnetic flux of 10^{-4} T, UV light of 1.085 W m^{-2}, and visible blue light of 1.5 W m^{-2}. For n-type LiG/CuO_x, the presence of CuO nanoparticles selectively reacts with blue visible light, demonstrating a normalized current gain maximum of +0.9 as presented in Fig. 7a. Subjection to the remaining stimuli was confined to a normalized gain of ±0.3. However, interestingly, the resistance immediately decreased to its neutral state despite continuous light exposure. The gradual change in sensor output over time could be due to aging, temperature, humidity, or other environmental factors.[83,84] A p-type LiG/CuO_x sensor reacted similarly but with a decrease in current output with a normalized current gain of −0.4. Other stimulants also did not indicate a significant current gain, suggesting an adequate selectivity of light for LiG/CuO_x sensors.

In Fig. 7b, a n-type LiG/ZnO_x sensor showed a normalized current gain of 0.21 to UV light but an indifference to the other stimuli nearing a 0 normalized current gain. The p-type LiG/ZnO_x presents a comparable result with a normalized gain of −0.12 under UV light and <0.05 for the rest of the stimuli. The UV light selectivity of LiG/ZnO_x is greater than the visible light selectivity of LiG/CuO_x.[85]

Fig. 7c shows an n-type LiG/FeO_x exhibited a great normalized current gain of 1.08 to a magnetic field. Contrasting the other transition metal oxides, the aligned FeO_x could retain the alignment after the removal of the external magnetic field.[7,86] The p-type LiG/FeO_x also behaves similarly with a −2.7 normalized current gain.

3.6 Flexible sensor demonstration

The LiG/MO_x sensors are designed for fingertips, as illustrated in Fig. 8a. These sensors, using PI film as a substrate, can contour to meet the weight, flexibility, durability, multi-
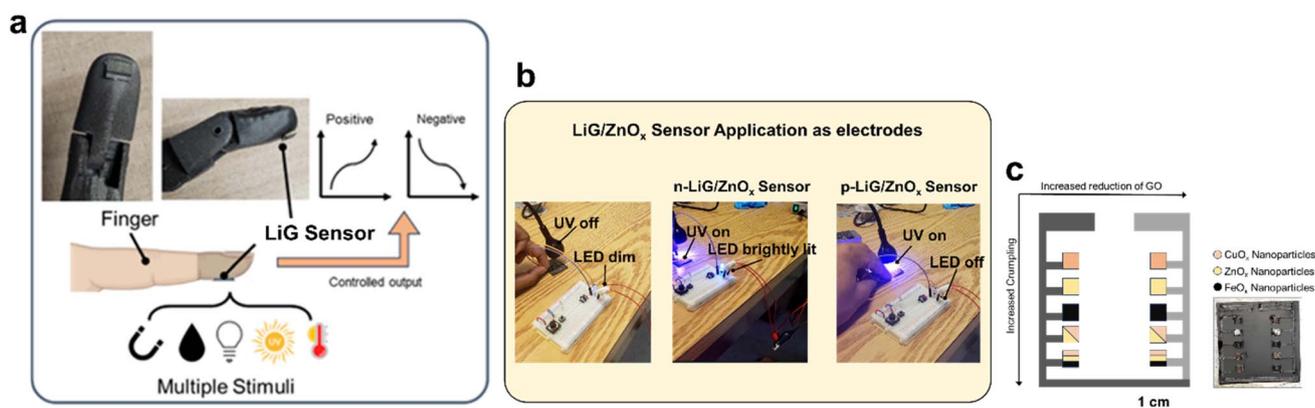

Fig. 8 Demonstration of different sensors. (a) Schematic of LiG/MO_x sensor application on a mechanical finger. (b) Applying as electrode for LiG/ZnO_x sensors. (c) Schematic and photo of a multifunctional LiG/MO_x sensor grid.

deformation, stretching, twisting, bending, and compression requirements of the biological body. Fig. 8b demonstrates the effective applicability of LiG/MO$_x$ films as laser-treated-electrodes. In a series circuit, where the LiG/ZnO$_x$ acts as an electrode, the tunable current gain under UV light is evident. For the n-type LiG/ZnO$_x$ film, when subjected to a UV light stimulus of 1.085 W m^{-2}, the sensor's resistance will decrease. As a result, the LED in the circuit will increase in brightness due to the higher conductivity. Conversely, when a p-type LiG/ZnO$_x$ is exposed to the same UV illumination, the sensor's resistance will increase, lowering the current enough to turn off the LED light. Lastly, Fig. 8c illustrates a proof-of-concept sensor grid that combines all 3 metal oxides to highlight the versatility and tunability of fLDW. The LiG layer mimics electrodes and placements of the positive and negative terminals will modify electron transport through the sensor. Effectively, increased reduction of GO and crumpling can contour sensor outputs based on probe placements, while nanoparticle components can provide sensing of selective stimuli.

3.6.1. LiG temperature sensors. The next figures highlight the strength, and more importantly, the exceptional tunability of the LiG/MO$_x$ sensor. First, Fig. 9a provides the current output of a LiG sensor, without metal/metal-oxide nanoparticles, under 1 V bias. There is a minor oscillation in the current output over time without any stimuli. The LiG shows a stable increase in conductivity with temperature growth, as illustrated in Fig. 9b. The innate temperature sensing of graphene membranes due to the density of states (DoS) near Fermi energy allows the LiG sensor to respond to temperature variation.[66] The temperature gradient adds either electrons or holes to the graphene channel, leading to an increase in conductivity. It shows great stability and recovery within the temperature range of 27–45 °C. Furthermore, the sensor recovers to its original resistive state in 0.08 seconds after turning off the heat source. The LiG exhibits applicability for skin-inspired sensors to monitor body temperature.[47]

3.6.2. LiG/ZnO$_x$ UV sensors. A p-type LiG/ZnO$_x$ and n-type LiG/ZnO$_x$ sensor were attached to a mechanical finger. The response of the sensor was gauged at variable distances from
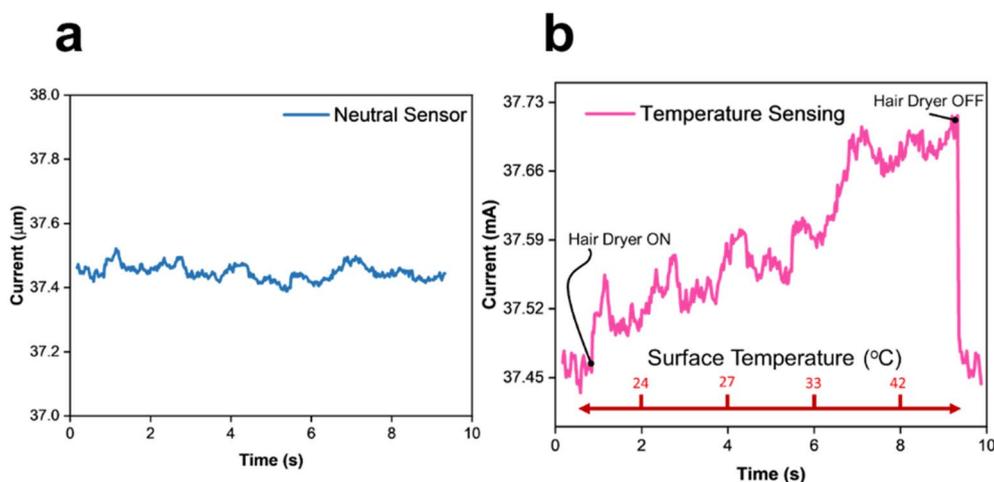

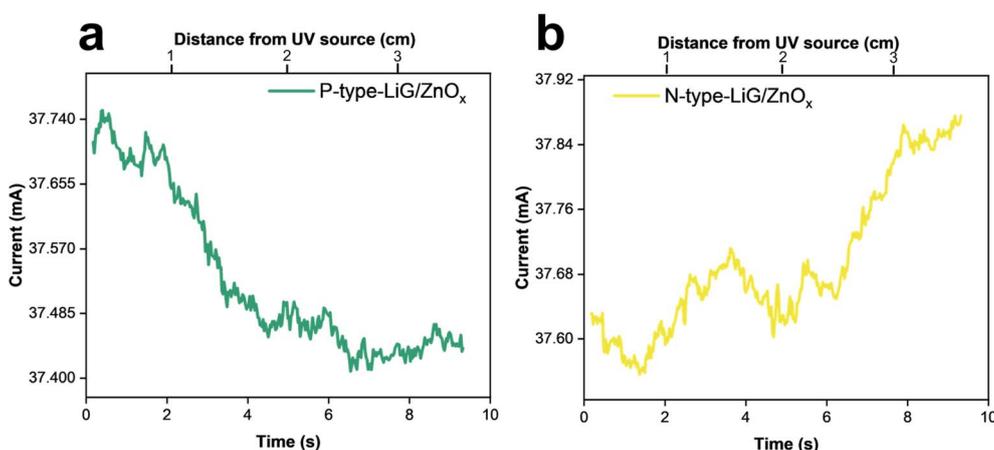**Fig. 9** (a) LiG sensor 1 V bias without stimuli (b) temperature response of LiG sensor.

Fig. 10 UV responses of (a) p-type and (b) n-type, LiG/ZnO$_x$ sensors.

a UV light source of 1.085 W m^{-2} intensity. fLDW highlights stability in sensor fabrication, as both sensors exhibited a consistent resistance gradient, as illustrated in Fig. 10a and b. The p-type sensor's current output decreased by 0.34 mA, whereas the n-type has an output increased by 0.32 mA, at a maximum distance of 3 cm from the UV source. The test mimics by what means LiG/MO$_x$ sensors, produced by fLDW, can be used to create tunable positive and negative sensors for fingertips to be used for proximity sensing.

3.6.3. LiG/CuO$_x$ light sensors. Fig. 11a and b presents the visible light response of p-type and n-type LiG/CuO$_x$ sensors. The p-type sensor current output decreased by 0.26 mA when subjected to blue light and by 0.18 mA under red light. The sensor showed selectivity to LEDs of different intensities. Similarly, the n-type sensor showed an increase in current output of 0.32 mA under blue light and 0.26 mA under red light. The sensors showed a low recovery time of < 0.2 s after the first LED was turned off; however, after the second LED, the sensor retained its new resistive state – a factor of rGO electron saturation, the recovery time was greatly affected by multiple sensor inputs.[30,60,87] This demonstrates the capability of fLDW to create

light sensors that can distinguish between lights of different intensities.

3.6.4. LiG humidity sensors. Additionally, the LiG/MO$_x$ sensors were placed in a 95% humidity chamber for extended durations and their changes in resistance. P-type LiG/CuO$_x$ (in Fig. 12a) showed the greatest resistance increase from 2.2 kΩ to 3.1 kΩ after 10 minutes in the humidity chamber. Similar to the visible light sensing of LiG/CuO$_x$, the conductivity nature of the LiG dictates whether the sensor increases or decreases in resistance when affected by humidity.[26] Likewise, the n-type-LiG/CuO$_x$ decreases in resistance the largest from 2.3 kΩ to 1.1 kΩ after 10 elapsed minutes as shown in Fig. 12b. The other nanoparticles had a minimal response to humidity.

3.6.5. LiG sensor performance and durability tests. Table 1 compares the performance of LiG/MO$_x$ sensors with similar flexible sensors, demonstrating that the LiG/MO$_x$ sensors offer a comparable response. For example, the UV response of LiG/ZnO$_x$ films shows a current of 7.13 μA at 1 V, which is comparable to the 5.5 μA at 1.5 V observed for ZnO/ethyl cellulose films. However, the key advantage of the fLDW technique is its greater customizability of the physical properties of the sensor. For instance, the
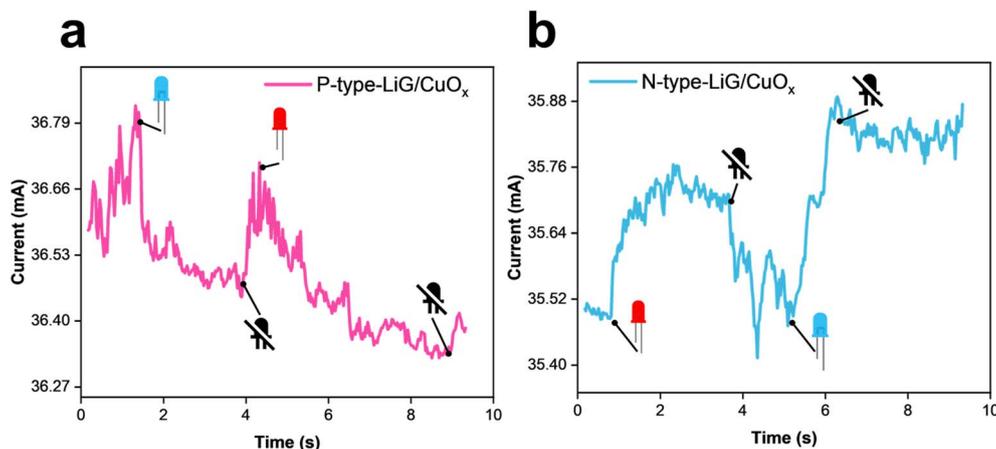

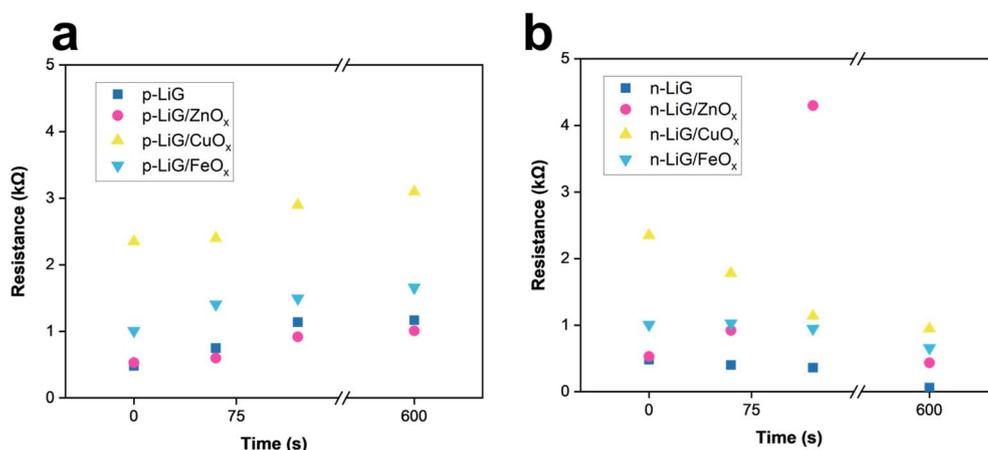**Fig. 11** Visible light responses of (a) p-type and (b) n-type LiG/CuO$_x$ sensors.

Fig. 12 Humidity responses of (a) p-type and (b) n-type LiG/MO$_x$ sensors.

responsivity of the LiG/ZnO$_x$ UV sensor can be tuned between 0.2 and 6 s, while an Al-nitride-nanowire UV sensor operates within a narrower range of 0.27 to 0.41 s. This flexibility in adjusting sensor response times and response intensity offers significant advantages in designing sensors for specific applications.

Table 2 shows the resilience of wearable LiG sensors; compared to various flexible photodetectors, LEDs, and gas sensors to evaluate their durability under challenging conditions via bend tests and performance assessment after 200 days in air. Bend tests were conducted with a bending radius of approximately 4.02 mm, resulting in a calculated surface strain of 5.001.[97] Impressively, the LiG/MO$_x$ sensors showed minimal degradation after 200 days in the air, maintaining normalized current gains at 70–80%, response times at 91–98%, and recovery times at 91% of initial values. This consistent performance was observed across all metal oxides integrated into the graphene matrix, suggesting the protective nature of dense porous films produced from fLDW against residual oxidation of metal species in reactive environments,[98] thereby preserving normalized response over extended periods.

However, a discrepancy was noted in performance degradation between normalized current and response/recovery times following bend tests. After 1000 bend cycles, normalized current gain decreased to 40–50%, further declining to 43–46% after 8000 bend cycles. In contrast, recovery and response times only degraded to 90–93% after 1000 bend cycles and 81–94% after 8000 bend cycles. The initial steep degradation in performance after 1000 cycles suggests that the TI surface layers weakly bonded on devices are unable to withstand bend cycles, leading to fractures and defects with low conductivity.[99] Conversely, the minimal reduction in performance after 1000 cycles suggests that the thicker LiG film, strongly bonded to the PI film, is more resilient to mechanical stressors. After the initial drop, the performance remains relatively stable. Furthermore, the programmable morphology, oxidation, crumpling, and doping characteristics

Table 1 Performance evaluation of LiG sensors and other flexible sensors

Type of sensor/device	Materials	Evaluation metric	Performance	Ref.	This work
Photosensor	Perylene/graphene	Resistance in dark	~5 MΩ	88	~4 MΩ LiG/CuO$_x$
UV photodetector	Al-nitride-nanowire	Responsivity	0.27–0.41 s to UV light illumination	89	0.2–6 s based on LiG/ZnO$_x$ crumpling
Flexible photodetector	Ti$_3$C$_2$T$_x$	Photoresponse	3.06 mA W^{-1}	90	0.21 mA per W LiG/CuO$_x$
UV sensor	ZnO/ethyl cellulose	Resistance	5.5 μA at 1.5 V	91	7.13 μA at 1 V LiG/ZnO$_x$
Light photodetector	Graphene/amorphous Ga$_2$O$_3$	Photocurrent	~10^5 photo-to-dark ratio	92	10–10^4 photo-to-dark LiG/CuO$_x$

Table 2 Endurance test summary of LiG sensors and other flexible sensors

Type of sensor/device	Materials	Evaluation metric	Performance change after endurance tests (% initial)	Ref.
Temperature sensor	Ni/NiO	Temperature coefficient of resistance (TCR)	21.9% after 8000 bend tests	93
Wearable LED	Ag NPs/PDMS	Luminance	82% after 300 bend cycles	94
Photosensor	Perylene/graphene	Resistance	93% after 1000 bend cycles	88
UV exposure sensor	Ortho-nitro benzyl	Yellowness index change (Y$_1$)	88% after 3.8 mm bend for 1 hour	95
Gas sensor	rGO/cotton-yarn	Normalized response (R$_n$)	94% after 1000 bend cycles 98% after 7 days of washing	96
UV photodetector	Al-nitride-nanowire	Responsivity	75% after 100 bend cycles	89
Flexible photodetector	Ti$_3$C$_2$T$_x$	Photoresponse	80% after 1000 bend cycles	90
UV sensor	ZnO/ethyl cellulose	Resistance	91% after 100 bend cycles	91
Light photodetector	Graphene/amorphous Ga$_2$O$_3$	Photocurrent	80% after 1000 bend cycles	92

Type of sensor/device	Materials	Evaluation metric		200 days in air	200 days w/1000 bend cycles	200 days w/8000 bend cycles	Ref.
			Performance change after endurance tests (% initial)				
Variety of resistive sensors	LiG/MO$_x$	Various	LiG/CuO$_x$ normalized current gain	80%	50%	46%	This work
			LiG/CuO$_x$ response time	98%	93%	94%	
			LiG/ZnO$_x$ normalized current gain	70%	40%	43%	
			LiG/ZnO$_x$ response time	91%	90%	81%	
			LiG/FeO$_x$ recovery time	91%	90%	81%	

of LiG produced by fLDW are robust, as these properties changed minimally in air and after bend cycles.[87,100]

4 Conclusion

In conclusion, a novel fLDW process was used to rapidly fabricate and combine reduced graphene and metal oxide nanoparticles to produce different sensors for the large-scale production of flexible electronics. Selectivity to humidity, visible light, UV light, and magnetic fluxes was demonstrated by LiG/CuO_x, LiG/ZnO_x, and LiG/FeO_x, respectively. The deposition mechanism, enabled by laser parameter modifications, allowed for simultaneous surface engineering of the LiG, including sp^2-carbon fractionization, 3D crumpling of rGO sheets, and for modifying the composition of metal oxides to tune the electrical properties of LiG/MO_x sensors. The normalized current gains were controllable by adjusting metal oxide nanoparticle compositions and sp^2 carbon fraction, ranging from -2.7 to 2.7. Response times were effectively modified by inducing crumpling structures on rGO sheets, varying from 0.02 to 3.5 seconds. Similarly, recovery times could be manipulated within the range of 2 to 6 seconds. The versatility of fLDW is further underscored by the fabrication of a flexible device featuring tunable LiG/MO_x sensors on polyimide substrates. These sensors are designed to conform to the requirements of biological bodies, displaying potential for personalized and adaptable sensing applications. Additionally, the programmable properties exhibited remarkable endurance even after 200 days in air and through numerous extended bend cycles. This advancement not only addresses challenges associated with traditional production methods but also offers exceptional controllability in selectivity, response time, recovery time, reproducibility, and stability.

Data availability

Data for this article is available at Zenodo at https://doi.org/10.5281/zenodo.14299824.

Conflicts of interest

The authors declare that they have no conflicts of interest regarding the publication of this article.

Acknowledgements

References

1 K. Xu, Y. Lu, K. Takei, K. Xu, Y. Lu and K. Takei, Multifunctional Skin-Inspired Flexible Sensor Systems for Wearable Electronics Flexible Wearable Sensors, *Adv. Mater. Technol.*, 2019, 1800628, DOI: 10.1002/admt.201800628.

2 T. Q. Trung and N. E. Lee, Flexible and Stretchable Physical Sensor Integrated Platforms for Wearable Human-Activity Monitoringand Personal Healthcare, *Adv. Mater.*, 2016, 28(22), 4338–4372, DOI: 10.1002/ADMA.201504244.

3 R. C. Webb, A. P. Bonifas, A. Behnaz, Y. Zhang, K. J. Yu, H. Cheng, M. Shi, Z. Bian, Z. Liu, Y. S. Kim, W. H. Yeo, J. S. Park, J. Song, Y. Li, Y. Huang, A. M. Gorbach and J. A. Rogers, Ultrathin Conformal Devices for Precise and Continuous Thermal Characterization of Human Skin, *Nat. Mater.*, 2013, 12(10), 938–944, DOI: 10.1038/nmat3755.

4 A. Nag, S. C. Mukhopadhyay and J. Kosel, Wearable Flexible Sensors: A Review, *IEEE Sens. J.*, 2017, 17(13), 3949–3960, DOI: 10.1109/JSEN.2017.2705700.

5 S. K. Chittibabu, K. Chintagumpala and A. Chandrasekhar, Porous Dielectric Materials Based Wearable Capacitance Pressure Sensors for Vital Signs Monitoring: A Review, *Mater. Sci. Semicond. Process.*, 2022, 151, 106976, DOI: 10.1016/J.MSSP.2022.106976.

6 M. Iversen, M. Monisha and S. Agarwala, Flexible, Wearable and Fully-Printed Smart Patch for PH and Hydration Sensing in Wounds, *Int. J. Bioprint.*, 2022, 8(1), 41–49, DOI: 10.18063/IJB.V8I1.447.

7 J. M. George, A. Antony and B. Mathew, Metal Oxide Nanoparticles in Electrochemical Sensing and Biosensing: A Review, *Mikrochim Acta*, 2018, 358, DOI: 10.1007/s00604-018-2894-3.

8 S. Zhu, D. Kim and C. Jeong, Recent Development of Mechanical Stimuli Detectable Sensors, Their Future, and Challenges: A Review, *Sensors*, 2023, 23(9), 4300, DOI: 10.3390/S23094300.

9 J. Dai, O. Ogbeide, N. Macadam, Q. Sun, W. Yu, Y. Li, B. L. Su, T. Hasan, X. Huang and W. Huang, Printed Gas Sensors, *Chem. Soc. Rev.*, 2020, 49(6), 1756–1789, DOI: 10.1039/C9CS00459A.

10 Y. Yoon, P. L. Truong, D. Lee and S. H. Ko, Metal-Oxide Nanomaterials Synthesis and Applications in Flexible and Wearable Sensors, *ACS Nanosci. Au*, 2022, 2(2), 64–92, DOI: 10.1021/ACSNANOSCIENCEAU.1C00029/ASSET/IMAGES/LARGE/NG1C00029_0014.JPEG.

11 D. T. Phan and G. S. Chung, P–n Junction Characteristics of Graphene oxide and Reduced Graphene oxide on n-Type Si(111), *J. Phys. Chem. Solids*, 2013, 74(11), 1509–1514, DOI: 10.1016/J.JPCS.2013.02.007.

12 K. Kim, H. B. R. Lee, R. W. Johnson, J. T. Tanskanen, N. Liu, M. G. Kim, C. Pang, C. Ahn, S. F. Bent and Z. Bao, Selective Metal Deposition at Graphene Line Defects by Atomic Layer Deposition, *Nat. Commun.*, 2014, 5(1), 1–9, DOI: 10.1038/ncomms5781.

13 B. Zhang, F. Zhang, F. Saba and C. Shang, Graphene-TiC Hybrid Reinforced Titanium Matrix Composites with 3D Network Architecture: Fabrication, Microstructure and Mechanical Properties, *J. Alloys Compd.*, 2021, 859, 157777, DOI: 10.1016/J.JALLCOM.2020.157777.

14 A. Moafi, O. Heidari, B. Soltannia, W. Wlodarski, F. Shahi and P. Parvin, Reduction of Metal Nanoparticle Decorated Flexible Graphene oxide by Laser at Various Temperatures

and under Selected Atmospheres, *Carbon Trends*, 2022, **6**, 100140, DOI: **10.1016/J.CARTRE.2021.100140**.

15 Y. Guo, C. Zhang, Y. Chen and Z. Nie, Research Progress on the Preparation and Applications of Laser-Induced Graphene Technology, *Nanomaterials*, 2022, **12**(14), 2336, DOI: **10.3390/NANO12142336**.

16 Y. Yang, S. Li, W. Yang, W. Yuan, J. Xu and Y. Jiang, In Situ Polymerization Deposition of Porous Conducting Polymer on Reduced Graphene oxide for Gas Sensor, *ACS Appl. Mater. Interfaces*, 2014, **6**(16), 13807–13814, DOI: **10.1021/AM5032456/ASSET/IMAGES/LARGE/AM-2014-032456_0016.JPEG**.

17 N. K. Elumalai and A. Uddin, Open Circuit Voltage of Organic Solar Cells: An in-Depth Review, *Energy Environ. Sci.*, 2016, **9**(2), 391–410, DOI: **10.1039/c5ee02871j**.

18 K. Janeczek, Composite Materials for Printed Electronics in Internet of Things Applications, *Bull. Mater. Sci.*, 2020, **43**(1), 1–10, DOI: **10.1007/S12034-020-02101-X/FIGURES/7**.

19 N. M. S. Hidayah, W. W. Liu, C. W. Lai, N. Z. Noriman, C. S. Khe, U. Hashim and H. C. Lee, Comparison on Graphite, Graphene oxide and Reduced Graphene oxide: Synthesis and Characterization, *AIP Conf. Proc.*, 2017, **1892**(1), 150002, DOI: **10.1063/1.5005764/965987**.

20 Y. Chen, Q. L. Zhu, N. Tsumori and Q. Xu, Immobilizing Highly Catalytically Active Noble Metal Nanoparticles on Reduced Graphene oxide: A Non-Noble Metal Sacrificial Approach, *J. Am. Chem. Soc.*, 2015, **137**(1), 106–109, DOI: **10.1021/JA511511Q/SUPPL_FILE/JA511511Q_SI_001.PDF**.

21 C. A. Amadei, P. Arribas and C. D. Vecitis, Graphene oxide Standardization and Classification: Methods to Support the Leap from Lab to Industry, *Carbon*, 2018, **133**, 398–409, DOI: **10.1016/J.CARBON.2018.02.091**.

22 S. Rathod, M. Snowdon, J. Jones, K. Zhang and P. Peng, In Situ Rapid Fabrication of Graphene−Copper Heterojunctions Using Fiber Laser Direct Writing, *ACS Appl. Mater. Interfaces*, 2023, **15**, 57326, DOI: **10.1021/acsami.3c11552**.

23 J. Jones, M. R. Snowdon, S. Rathod and P. Peng, Direct Laser Writing of Copper and Copper Oxide Structures on Plastic Substrates for Memristor Devices, *Flexible Printed Electron.*, 2023, **8**(1), 015008, DOI: **10.1088/2058-8585/acb0df**.

24 W. Zhou, Y. Yu, S. Bai and A. Hu, Laser Direct Writing of Waterproof Sensors inside Flexible Substrates for Wearable Electronics, *Opt. Laser Technol.*, 2021, **135**, 106694, DOI: **10.1016/J.OPTLASTEC.2020.106694**.

25 S. Rathod, M. Snowdon, J. Jones, K. Zhang and P. Peng, In Situ Rapid Fabrication of Graphene–Copper Heterojunctions Using Fiber Laser Direct Writing, *ACS Appl. Mater. Interfaces*, 2023, **15**, 57326, DOI: **10.1021/ACSAMI.3C11552**.

26 X. Zhou, W. Guo, J. Fu, Y. Zhu, Y. Huang and P. Peng, Laser Writing of Cu/Cu$_x$O Integrated Structure on Flexible Substrate for Humidity Sensing, *Appl. Surf. Sci.*, 2019, **494**, 684–690, DOI: **10.1016/J.APSUSC.2019.07.159**.

27 S. D. Afonnikova, A. A. Popov, Y. I. Bauman, P. E. Plyusnin, I. V. Mishakov, M. V. Trenikhin, Y. V. Shubin, A. A. Vedyagin and S. V. Korenev, Porous Co-Pt Nanoalloys for Production of Carbon Nanofibers and Composites, *Materials*, 2022, **15**(21), 7456, DOI: **10.3390/MA15217456**.

28 C. Zhu, S. Guo, Y. Fang and S. Dong, Reducing Sugar: New Functional Molecules for the Green Synthesis of Graphene Nanosheets, *ACS Nano*, 2010, 2429–2437, DOI: **10.1021/nn1002387**.

29 H.-L. Ma, H.-B. Zhang, Q.-H. Hu, W.-J. Li, Z.-G. Jiang, Z.-Z. Yu and A. Dasari, Functionalization and Reduction of Graphene oxide with P-Phenylene Diamine for Electrically Conductive and Thermally Stable Polystyrene Composites, *ACS Appl. Mater. Interfaces*, 2012, 1948–1953, DOI: **10.1021/am201654b**.

30 A. Mondal, A. Prabhakaran, S. Gupta and V. R. Subramanian, Boosting Photocatalytic Activity Using Reduced Graphene oxide (RGO)/Semiconductor Nanocomposites: Issues and Future Scope, *ACS Omega*, 2021, **6**(13), 8734–8743, DOI: **10.1021/ACSOMEGA.0C06045/ASSET/IMAGES/LARGE/AO0C06045_0003.JPEG**.

31 T. W. P. Seadira, C. M. Masuku and M. S. Scurrell, Solar Photocatalytic Glycerol Reforming for Hydrogen Production over Ternary Cu/THS/Graphene Photocatalyst: Effect of Cu and Graphene Loading, *Renew. Energy*, 2020, 84–97, DOI: **10.1016/j.renene.2020.04.020**.

32 A. Rashid, M. Yusoff, W. Jose Da Silva and F. K. Schneider, Understanding the PH-Dependent Behaviour of Graphene oxide Aqueous Solutions on Organic Photovoltaic Performance, *Sol. Energy Mater. Sol. Cell.*, 2019, 62–66, DOI: **10.1016/j.solmat.2019.01.045**.

33 A. K. Tolkou and A. I. Zouboulis, Graphene oxide/Fe-Based Composite Pre-Polymerized Coagulants: Synthesis, Characterization, and Potential Application in Water Treatment, *C*, 2020, 44, DOI: **10.3390/c6030044**.

34 N. Sezer, A. Ali, M. A. Atieh and M. Koc, Synthesis and Characterization of Graphene/Zinc Oxide Nanocomposites, *Proceedings of the ASME 2017 International Mechanical Engineering Congress and Exposition*, Volume 8: Heat Transfer and Thermal Engineering, ASME, Tampa, Florida, USA, 2018, DOI: **10.1115/IMECE2017-71291**.

35 A. Trakic, N. Eskandarnia, B. Keong Li, K. W. J Wong, M. R. Field, J. Zhen Ou, K. Latham, M. J. S Spencer, I. Yarovsky and K. Kalantar-zadeh, Interaction of Hydrogen with ZnO Nanopowders-Evidence of Hydroxyl Group Formation You May Also like Phase-Space Tomography for Characterization of Rotationally Symmetric Beams A Cámara, T Alieva, I Castro *et al.* -Rotational Magnetic Induction Tomography Interaction of Hydrogen with ZnO Nanopowders-Evidence of Hydroxyl Group Formation, *Nanotechnology*, 2012, **23**, 7, DOI: **10.1088/0957-4484/23/1/015705**.

36 H. Li, L. Zhang, H. Lu, J. Ma, X. Zhou, Z. Wang and C. Yi, Macro-/Nanoporous Al-Doped ZnO/Cellulose Composites Based on Tunable Cellulose Fiber Sizes for Enhancing Photocatalytic Properties, *Carbohydr. Polym.*, 2020, 116873, DOI: **10.1016/j.carbpol.2020.116873**.

37 M. J. Robles-águila, J. A. Luna-López, Á. D. Hernández de la Luz, J. Martínez-Juárez and M. E. Rabanal, Synthesis and Characterization of Nanocrystalline ZnO Doped with Al3+ and Ni2+ by a Sol–Gel Method Coupled with Ultrasound Irradiation, *Crystals*, 2018, **8**(11), 406, DOI: **10.3390/CRYST8110406**.

38 Y. Wang, L. Liu, Y. Cai, J. Chen and J. Yao, Preparation and Photocatalytic Activity of Cuprous Oxide/Carbon Nanofibres Composite Films, *Appl. Surf. Sci.*, 2013, **270**, 245–251, DOI: **10.1016/j.apsusc.2013.01.011**.

39 S. B. Khan, K. Akhtar, E. M. Bakhsh and A. M. Asiri, Electrochemical Detection and Catalytic Removal of 4-Nitrophenol Using CeO2-Cu2O and CeO2-Cu2O/CH Nanocomposites, *Appl. Surf. Sci.*, 2019, 726–735, DOI: **10.1016/j.apsusc.2019.06.205**.

40 T. W. P. Seadira, C. M. Masuku and M. S. Scurrell, Solar Photocatalytic Glycerol Reforming for Hydrogen Production over Ternary Cu/THS/Graphene Photocatalyst: Effect of Cu and Graphene Loading, *Renewable Energy*, 2020, **156**, 84–97, DOI: **10.1016/J.RENENE.2020.04.020**.

41 J. A. Torres-Ochoa, D. Cabrera-German, O. Cortazar-Martinez, M. Bravo-Sanchez, G. Gomez-Sosa and A. Herrera-Gomez, Peak-Fitting of Cu 2p Photoemission Spectra in Cu0, Cu1+, and Cu2+ Oxides: A Method for Discriminating Cu0 from Cu1+, *Appl. Surf. Sci.*, 2023, **622**, 156960, DOI: **10.1016/J.APSUSC.2023.156960**.

42 H. Ju, N. Ding, J. Xu, L. Yu, Y. Geng, G. Yi and T. Wei, Improvement of Tribological Properties of Niobium Nitride Films *via* Copper Addition, *Vacuum*, 2018, 1–5, DOI: **10.1016/j.vacuum.2018.09.037**.

43 S. B. Khan, K. Akhtar, E. M. Bakhsh and A. M. Asiri, Electrochemical Detection and Catalytic Removal of 4-Nitrophenol Using CeO2-Cu2O and CeO2-Cu2O/CH Nanocomposites, *Appl. Surf. Sci.*, 2019, **492**, 726–735, DOI: **10.1016/J.APSUSC.2019.06.205**.

44 N. M. El-Shafai, N. A. Alamrani, A. M. Al-Bonayan C, S. Abu-Melha, N. M. El-Metwaly and I. El-Mehasseb, Building Electrons Clouds of Redesigned Copper Oxide Nanorods Captured on the Graphene oxide Surface for Supercapacitors and Energy Storage, *Surface. Interfac.*, 2023, **38**, 102757, DOI: **10.1016/j.surfin.2023.102757**.

45 D. Mardiansyah, T. Badloe, K. Triyana, M. Q. Mehmood, N. Raeis-Hosseini, Y. Lee, H. Sabarman, K. Kim and J. Rho, Effect of Temperature on the Oxidation of Cu Nanowires and Development of an Easy to Produce, Oxidation-Resistant Transparent Conducting Electrode Using a PEDOT:PSS Coating, *Sci. Rep.*, 2018, **8**, 10639, DOI: **10.1038/s41598-018-28744-9**.

46 H. Siddiqui, M. R. Parra, M. S. Qureshi, M. M. Malik and F. Z. Haque, Studies of Structural, Optical, and Electrical Properties Associated with Defects in Sodium-Doped Copper Oxide (CuO/Na) Nanostructures, *J. Mater. Sci.*, 2018, **53**(12), 8826–8843, DOI: **10.1007/S10853-018-2179-6/FIGURES/15**.

47 B. Davaji, H. D. Cho, M. Malakoutian, J. K. Lee, G. Panin, T. W. Kang and C. H. Lee, A Patterned Single Layer Graphene Resistance Temperature Sensor, *Sci. Rep.*, 2017, **7**(1), 1–10, DOI: **10.1038/s41598-017-08967-y**.

48 T. Kamakshi, G. S. Sundari, H. Erothu and T. P. Rao, Synthesis And Characterization of Graphene Based Iron Oxide (Fe3O4) Nanocomposites, *Rasayan J. Chem.*, 2018, **11**(3), 1113–1119, DOI: **10.31788/RJC.2018.1134003**.

49 I. S. Lyubutin, A. O. Baskakov, S. S. Starchikov, K.-Y. Shih, C.-R. Lin, Y.-T. Tseng, S.-S. Yang, Z.-Y. Han, Y. L. Ogarkova, V. I. Nikolaichik and A. S. Avilov, Synthesis and Characterization of Graphene Modified by Iron Oxide Nanoparticles, *Mater. Chem. Phys.*, 2018, 411–420, DOI: **10.1016/j.matchemphys.2018.08.042**.

50 R. Sun, H.-B. Zhang, J. Yao, D. Yang, Y.-W. Mai and Z.-Z. Yu, In Situ Reduction of Iron Oxide with Graphene for Convenient Synthesis of Various Graphene Hybrids, *Carbon*, 2016, 138–145, DOI: **10.1016/j.carbon.2016.05.041**.

51 Q. Zeng, High Temperature Low Friction Behavior of H-BN Coatings against ZrO2, *Coatings*, 2022, **12**(11), 1772, DOI: **10.3390/COATINGS12111772**.

52 H. Su, Z. Ye and N. Hmidi, High-Performance Iron Oxide-Graphene oxide Nanocomposite Adsorbents for Arsenic Removal, *Physicochem. Eng. Asp.*, 2017, **522**, 161–172, DOI: **10.1016/j.colsurfa.2017.02.065**.

53 V. Urbanova, M. Magro, A. Gedanken, D. Baratella, F. Vianello and R. Zboril, Nanocrystalline Iron Oxides, Composites, and Related Materials as a Platform for Electrochemical, Magnetic, and Chemical Biosensors, *Chem. Mater.*, 2014, **26**(23), 6653–6673, DOI: **10.1021/CM500364X/ASSET/IMAGES/LARGE/CM-2014-00364X_0036.JPEG**.

54 C. Zhou, L. Wan, Z. Lou, S. Wu, S. A. Baig and X. Xu, Comparative Sb(V) Removal Efficacy of Different Iron Oxides from Textile Wastewater: Effects of Co-Existing Anions and Dye Compounds, *Environ. Sci. Pollut. Res. Int.*, 2023, **30**(57), 120030–120043, DOI: **10.1007/S11356-023-30771-7/FIGURES/8**.

55 C. Xu, X. Wang and J. Zhu, Graphene - Metal Particle Nanocomposites, *J. Phys. Chem. C*, 2008, **112**(50), 19841–19845, DOI: **10.1021/JP807989B/SUPPL_FILE/JP807989B_SI_001.PDF**.

56 H. Yan, C. Lai, S. Liu, D. Wang, X. Zhou, M. Zhang, L. Li, X. Li, F. Xu and J. Nie, Metal-Carbon Hybrid Materials Induced Persulfate Activation: Application, Mechanism, and Tunable Reaction Pathways, *Water Res.*, 2023, **234**, 119808, DOI: **10.1016/J.WATRES.2023.119808**.

57 X. Liu, Y. Sui, C. Meng and Y. Han, Tuning the Reactivity of Ru Nanoparticles by Defect Engineering of the Reduced Graphene oxide Support, *RSC Adv.*, 2014, 22230–22240, DOI: **10.1039/c4ra02900c**.

58 G. Golan, A. Axelevitch, B. Gorenstein and V. Manevych, Hot-Probe Method for Evaluation of Impurities Concentration in Semiconductors, *Microelectron. J.*, 2006, **37**(9), 910–915, DOI: **10.1016/J.MEJO.2006.01.014**.

59 A. Omidvar and A. Mohajeri, Promotional Effect of the Electron Donating Functional Groups on the Gas Sensing Properties of Graphene Nanofakes, *RSC Adv.*, 2015, 54535–54543, DOI: **10.1039/c5ra10298g**.

60 A. Bin Rahaman, A. Sarkar, T. Singha, K. Chakraborty, S. Dutta, T. Pal, S. Ghosh, P. K. Datta and D. Banerjee, Electrical Transport Properties and Ultrafast Optical Nonlinearity of RGO-Metal Chalcogenide Ensembles, *Nanoscale Adv.*, 2020, 1573–1582, DOI: **10.1039/c9na00728h**.

61 N. Kang and S. I. Khondaker, The Impact of Carbon Sp2 Fraction of Reduced Graphene oxide on the Performance of Reduced Graphene oxide Contacted Organic Transistors, *Appl. Phys. Lett.*, 2014, **105**(22), 223301, DOI: **10.1063/1.4902881/12945545/223301_1_ACCEPTED_MANUSCRIPT.PDF**.

62 H. Shi, C. Wang, Z. Sun, Y. Zhou, K. Jin, S. A. T. Redfern and G. Yang, Tuning the Nonlinear Optical Absorption of Reduced Graphene oxide by Chemical Reduction, *Opt. Express*, 2014, **22**(16), 19375, DOI: **10.1364/oe.22.019375**.

63 N. D. K. Tu, J. Choi, C. R. Park and H. Kim, Remarkable Conversion between N- and p-Type Reduced Graphene oxide on Varying the Thermal Annealing Temperature, *Chem. Mater.*, 2015, **27**(21), 7362–7369, DOI: **10.1021/acs.chemmater.5b02999**.

64 R. Rudenko, O. Voitsihovska, A. Abakumov, I. Bychko, O. Selyshchev, D. R. T. Zahn and V. Poroshin, The Hopping Hall Effect in Reduced Graphene oxide, *Mater. Lett.*, 2022, **326**, 132932, DOI: **10.1016/J.MATLET.2022.132932**.

65 R. Haerle, E. Riedo, A. Pasquarello and A. Baldereschi, (Formula Presented) Hybridization Ratio in Amorphous Carbon from C (Formula Presented) Core-Level Shifts: X-Ray Photoelectron Spectroscopy and First-Principles Calculation, *Phys. Rev. B:Condens. Matter Mater. Phys.*, 2002, **65**(4), 1–9, DOI: **10.1103/PHYSREVB.65.045101**.

66 B. Saha, S. Baek and J. Lee, Highly Sensitive Bendable and Foldable Paper Sensors Based on Reduced Graphene oxide, *ACS Appl. Mater. Interfaces*, 2017, 4658–4666, DOI: **10.1021/acsami.6b10484**.

67 J. Li, T.-F. Chung, Y. P. Chen and G. J. Cheng, Nanoscale Strainability of Graphene by Laser Shock-Induced Three-Dimensional Shaping, *Nano Lett.*, 2012, 4577–4583, DOI: **10.1021/nl301817t**.

68 C. Coleman, R. Erasmus and S. Bhattacharyya, Nanoscale Deformations in Graphene by Laser Annealing, *Appl. Phys. Lett.*, 2016, **109**(25), 253102, DOI: **10.1063/1.4972845/32028**.

69 Z. Wang, X. Lv, Y. Chen, D. Liu, X. Xu, G. T. R. Palmore and R. H. Hurt, Crumpled Graphene Nanoreactors, *Nanoscale*, 2015, 7(22), 10267–10278, DOI: **10.1039/C5NR00963D**.

70 R. Liang, J. C. Van Leuwen, L. M. Bragg, M. J. Arlos, L. C. M. Li Chun Fong, O. M. Schneider, I. Jaciw-Zurakowsky, A. Fattahi, S. Rathod, P. Peng, M. R. Servos and Y. N. Zhou, Utilizing UV-LED Pulse Width Modulation on TiO2 Advanced Oxidation Processes to Enhance the Decomposition Efficiency of Pharmaceutical Micropollutants, *Chem. Eng. J.*, 2019, 439–449, DOI: **10.1016/j.cej.2018.12.065**.

71 H. Särkkä, M. Vepsäläinen and M. Sillanpää, Natural Organic Matter (NOM) Removal by Electrochemical Methods - A Review, *J. Electroanal. Chem.*, 2015, 100–108, DOI: **10.1016/j.jelechem.2015.07.029**.

72 Y. Xia, R. Li, R. Chen, J. Wang and L. Xiang, 3D Architectured Graphene/Metal Oxide Hybrids for Gas Sensors: A Review, *Sensors*, 2018, **18**(5), 1456, DOI: **10.3390/S18051456**.

73 X. Guo, C. Zhu, G. Xu and F. Cheng, Synergetic-Modified Porous Co2SiO4 Conductive Network with ZIF-8 Derived Carbon and Reduced Graphene oxide for High-Rate Lithium-Ion Battery Anode, *J. Electroanal. Chem.*, 2023, **941**, 117530, DOI: **10.1016/J.JELECHEM.2023.117530**.

74 X. Gao, Z. Tang, M. Meng, Q. Yu, Y. Zhu, S. Shen and J. Yang, Synthesis of Crumpled SnO2/RGO Nanocomposites with 2D-in-3D Structure and High Performance, *Mater. Chem. Phys.*, 2020, **253**, 123298, DOI: **10.1016/J.MATCHEMPHYS.2020.123298**.

75 Y. Z. Liu, C. M. Chen, Y. F. Li, X. M. Li, Q. Q. Kong and M. Z. Wang, Crumpled Reduced Graphene oxide by Flame-Induced Reduction of Graphite Oxide for Supercapacitive Energy Storage, *J. Mater. Chem. A*, 2014, **2**(16), 5730–5737, DOI: **10.1039/C3TA15082H**.

76 X. Gao, Z. Tang, M. Meng, Q. Yu, J. Li, S. Shen and J. Yang, Graphene oxide Induced Assembly and Crumpling of Co3O4 Nanoplates, *Nanotechnology*, 2020, **31**(30), 305601, DOI: **10.1088/1361-6528/AB841F**.

77 R. Suderman, D. J. Lizotte and N. M. Abukhdeir, Theory and Application of Shapelets to the Analysis of Surface Self-Assembly Imaging, *Phys. Rev. E:Stat., Nonlinear, Soft Matter Phys.*, 2015, **91**(3), 033307, DOI: **10.1103/PHYSREVE.91.033307/FIGURES/8/MEDIUM**.

78 M. P. Tino, A. Y. Abdulaziz, R. Suderman, T. Akdeniz and N. M. Abukhdeir, Shapelets: A Python Package Implementing Shapelet Functions and Their Applications, *J. Open Source Softw.*, 2024, **9**(95), 6058, DOI: **10.21105/JOSS.06058**.

79 X. Gao, Z. Tang, M. Meng, Q. Yu, Y. Zhu, S. Shen and J. Yang, Synthesis of Crumpled SnO 2/RGO Nanocomposites with 2D-in-3D Structure and High Performance, *Mater. Chem. Phys.*, 2020, **253**, 123298, DOI: **10.1016/j.matchemphys.2020.123298**.

80 M. Que, C. Lin, J. Sun, L. Chen, X. Sun and Y. Sun, Progress in ZnO Nanosensors, *Sensors*, 2021, **21**(16), 5502, DOI: **10.3390/S21165502**.

81 M. E. Franke, T. J. Koplin and U. Simon, Metal and Metal Oxide Nanoparticles in Chemiresistors: Does the Nanoscale Matter? From the Contents, *Small*, 2005, 36–50, DOI: **10.1002/smll.200500261**.

82 S. Goutham, S. Bykkam, K. K. Sadasivuni, D. Santhosh Kumar, M. Ahmadipour, Z. A. Ahmad and K. Venkateswara Rao, Room Temperature LPG Resistive Sensor Based on the Use of a Few-Layer Graphene/SnO2 Nanocomposite, *Mikrochim. Acta*, 2017, 69, DOI: **10.1007/s00604-017-2537-0**.

83 G. D. Renzone, E. Landi, M. Mugnaini, L. Parri, G. Peruzzi and A. Pozzebon, Assessment of LoRaWAN Transmission Systems under Temperature and Humidity, Gas, and Vibration Aging Effects Within IIoT Contexts, *IEEE Trans.*

Instrum. Meas., 2022, **71**, 1–11, DOI: **10.1109/TIM.2021.3137568**.

84 S. Garakyaraghi, C. E. McCusker, S. Khan, P. Koutnik, A. T. Bui and F. N. Castellano, Enhancing the Visible-Light Absorption and Excited-State Properties of Cu(I) MLCT Excited States, *Inorg. Chem.*, 2018, **57**(4), 2296–2307, DOI: **10.1021/ACS.INORGCHEM.7B03169/ASSET/IMAGES/LARGE/IC-2017-03169D_0004.JPEG**.

85 M. Y. Li, M. Yu, D. Su, J. Zhang, S. Jiang, J. Wu, Q. Wang and S. Liu, Ultrahigh Responsivity UV Photodetector Based on Cu Nanostructure/ZnO QD Hybrid Architectures, *Small*, 2019, **15**(28), 1901606, DOI: **10.1002/SMLL.201901606**.

86 I. Koh and L. Josephson, Magnetic Nanoparticle Sensors, *Sensors*, 2009, **9**(10), 8130–8145, DOI: **10.3390/S91008130**.

87 S. Deng and V. Berry, Wrinkled, Rippled and Crumpled Graphene: An Overview of Formation Mechanism, Electronic Properties, and Applications, *Mater. Today*, 2016, **19**(4), 97–212, DOI: **10.1016/j.mattod.2015.10.002**.

88 S. Ali, J. Bae and C. H. Lee, Stretchable Photo Sensor Using Perylene/Graphene Composite on Ridged Polydimethylsiloxane Substrate, *Opt. Express*, 2015, **23**(24), 30583–30591, DOI: **10.1364/OE.23.030583**.

89 Y. B. Ozdemir and K. Teker, Self-Powered High-Performance Flexible Aluminum Nitride Nanowire Deep Ultraviolet Photodetector, *IEEE Trans. Instrum. Meas.*, 2022, **128**(9), 1–8, DOI: **10.1007/S00340-022-07893-W/FIGURES/6**.

90 C. Xie, Y. Wang, Z. Xia, Y. Cheng, X. Cui, S. Xu, X. Ren, W. Yang and Z. Huang, High-Performance Broadband Flexible Photodetectors Based on Ti3C2Tx MXene/Pyramidal Thin Si Heterostructures with Light Trapping Effect for Heart Rate Detection, *Adv. Mater. Technol.*, 2023, **8**(24), 2301232, DOI: **10.1002/ADMT.202301232**.

91 J. Figueira, C. Gaspar, J. T. Carvalho, J. Loureiro, E. Fortunato, R. Martins and L. Pereira, Sustainable Fully Printed UV Sensors on Cork Using Zinc Oxide/Ethylcellulose Inks, *Micromachines*, 2019, **10**(9), 601, DOI: **10.3390/MI10090601**.

92 Y. Wang, Z. Yang, H. Li, S. Li, Y. Zhi, Z. Yan, X. Huang, X. Wei, W. Tang and Z. Wu, Ultrasensitive Flexible Solar-Blind Photodetectors Based on Graphene/Amorphous Ga2O3Van Der Waals Heterojunctions, *ACS Appl. Mater. Interfaces*, 2020, **12**(42), 47714–47720, DOI: **10.1021/ACSAMI.0C10259/SUPPL_FILE/AM0C10259_SI_001.PDF**.

93 A. B. Appiagyei, J. Banua and J. I. Han, Flexible and Patterned-Free Ni/NiO-Based Temperature Device on Cylindrical PET Fabricated by RF Magnetron Sputtering: Bending and Washing Endurance Tests, *J. Ind. Eng. Chem.*, 2021, **100**, 372–382, DOI: **10.1016/J.JIEC.2021.04.058**.

94 L. Veeramuthu, C. J. Cho, F. C. Liang, M. Venkatesan, R. Kumar G, H. Y. Hsu, R. J. Chung, C. H. Lee, W. Y. Lee and C. C. Kuo, Human Skin-Inspired Electrospun Patterned Robust Strain-Insensitive Pressure Sensors and Wearable Flexible Light-Emitting Diodes, *ACS Appl. Mater. Interfaces*, 2022, **14**(26), 30160–30173, DOI: **10.1021/ACSAMI.2C04916/SUPPL_FILE/AM2C04916_SI_003.MP4**.

95 M. E. Lee and A. M. Armani, Flexible UV Exposure Sensor Based on UV Responsive Polymer, *ACS Sens.*, 2016, **1**(10), 1251–1255, DOI: **10.1021/ACSSENSORS.6B00491/SUPPL_FILE/SE6B00491_SI_001.PDF**.

96 Y. J. Yun, W. G. Hong, N. J. Choi, B. H. Kim, Y. Jun and H. K. Lee, Ultrasensitive and Highly Selective Graphene-Based Single Yarn for Use in Wearable Gas Sensor, *Sci. Rep.*, 2015, **5**(1), 1–7, DOI: **10.1038/srep10904**.

97 R. Saleh, M. Barth, W. Eberhardt and A. Zimmermann, Bending Setups for Reliability Investigation of Flexible Electronics, *Micromachines*, 2021, **12**(1), 1–22, DOI: **10.3390/MI12010078**.

98 S. Chen, L. Brown, M. Levendorf, W. Cai, S. Y. Ju, J. Edgeworth, X. Li, C. W. Magnuson, A. Velamakanni, R. D. Piner, J. Kang, J. Park and R. S. Ruoff, Oxidation Resistance of Graphene-Coated Cu and Cu/Ni Alloy, *ACS Nano*, 2011, **5**(2), 1321–1327, DOI: **10.1021/NN103028D/ASSET/IMAGES/MEDIUM/NN-2010-03028D_0005.GIF**.

99 F. Hui, Y. Shi, Y. Ji, M. Lanza and H. Duan, Mechanical Properties of Locally Oxidized Graphene Electrodes, *Arch. Appl. Mech.*, 2015, **85**(3), 339–345, DOI: **10.1007/S00419-014-0957-4/METRICS**.

100 A. M. Díez-Pascual and A. Rahdar, Graphene-Based Polymer Composites for Flexible Electronic Applications, *Micromachines*, 2022, **13**(7), 1123, DOI: **10.3390/MI13071123**.